BPOP-v1 model: exploring the impact of changes in the biological pump on the shelf sea and ocean nutrient and redox state

Elisa Lovecchio[1] and Timothy M. Lenton[1]

[1]Global Systems Institute, University of Exeter, Exeter, EX4 4QE, United Kingdom

Correspondence to: Elisa Lovecchio (e.lovecchio@exeter.ac.uk)

Abstract. The ocean's biological pump has changed over Earth history from one dominated by prokaryotes, to one involving a mixture of prokaryotes and eukaryotes with trophic structure. Changes in the biological pump are in turn hypothesised to have caused important changes in the ocean's nutrient and redox properties. To explore these hypotheses, we present here a new box model including oxygen (O), phosphorus (P) and a dynamical biological pump. Our Biological Pump, Oxygen and Phosphorus (BPOP) model accounts for two – small and large – organic matter species generated by production and coagulation, respectively. Export and burial of these particles are regulated by a remineralization length (z_{rem}) scheme. We independently vary z_{rem} of small and large particles in order to study how changes in sinking speeds and remineralization rates affect the major biogeochemical fluxes, and O and P ocean concentrations. Modelled O and P budgets and fluxes lie reasonably close to present estimates for z_{rem} in the range of currently measured values. Our results highlight that relatively small changes in z_{rem} of the large particles can have important impacts on the O and P ocean availability and support the idea that an early ocean dominated by small particles was nutrient rich due to inefficient removal to sediments. The results also suggest that extremely low oxygen concentrations in the shelf can coexist with an oxygenated deep open ocean for realistic values of z_{rem}, especially for large values of the small particle z_{rem}. This could challenge conventional interpretations that the Proterozoic deep ocean was anoxic, which are derived from shelf and slope sediment redox data. This simple and computationally inexpensive model is a promising tool to investigate the impact of changes in the organic matter sinking and remineralization rates as well as changes in physical processes coupled to the biological pump in a variety of case studies.

1 Introduction

The 'biological pump' describes the production of organic matter at the ocean's surface (an oxygen source), its downward export/sinking flux, remineralisation at depth (an oxygen sink), and burial. This set of processes acts against the homogenization of tracer concentrations by the ocean's circulation, maintaining large-scale tracer gradients (Sarmiento and Gruber, 2006). In today's world, the biological pump plays a key role in transferring carbon from the atmosphere/surface ocean to the deep ocean and in so doing lowers atmospheric CO_2 and creates oxygen demand in deeper waters (Lam et al., 2011;Kwon et al., 2009). Those deeper waters with the greatest oxygen demand relative to oxygen supply can be driven hypoxic (O_2 < 60 mmol m^{-3}), suboxic (O_2 < 5 mmol m^{-3}) or even anoxic – as is being seen in parts of the ocean today (Keeling et al., 2010). By combining surface oxygen production and organic carbon burial, the biological pump plays a role in determining the long-term source of oxygen to the atmosphere. The biological pump also provides a means of efficiently transferring organic matter

and the nutrients it contains to marine sediments, if sinking through the water column happens fast enough compared to remineralization for the material to hit the bottom (Sarmiento and Gruber, 2006). Hence the biological pump plays a key part in balancing the input of phosphorus to the ocean with a corresponding output flux of phosphorus buried in marine sediments.

Through Earth's history, the characteristics, efficiency and impact of the biological pump are thought to have changed dramatically due to the evolution of increasingly large and complex marine organisms (Ridgwell, 2011;Logan et al., 1995;Boyle et al., 2018). Life in the ocean began as just prokaryotes, presumably attacked by viruses, with slow sinking of the resulting tiny particles. Now the marine ecosystem is a mix of prokaryotic cyanobacteria and heterotrophs, and size-structured eukaryotic algae, mixotrophs and heterotrophs all the way up to large jellyfish, fish and whales. Some of the resulting particles sink very fast (McDonnell and Buesseler, 2010). How changes in the biological pump have affected ocean nutrient and redox state at different times in Earth history is a subject of active research and hypothesis generation. Previous work has highlighted the Neoproterozoic Era, spanning from 1,000 to 541 million years ago, as of particular interest because it saw a shift of dominance from prokaryotes to eukaryotes and a series of dramatic shifts in the climate, biogeochemical cycling and ocean redox state (Katz et al., 2007;Brocks et al., 2017). A common paradigm has been to assume that a progressive rise of oxygen in the atmosphere (of uncertain cause) drove the oxygenation of the deep ocean at this time through air-sea gas exchange and mixing, but equally increases in the efficiency of the biological pump could have lowered ocean phosphorus concentration and thus oxygenated the ocean (Lenton et al., 2014). Recent data show a series of transient ocean oxygenation events ~660-520 Ma, which get more frequent over time, suggesting a complex interplay of processes on multiple timescales, including changes in the biological pump and ocean phosphorus inventory (Lenton and Daines, 2018).

During the Phanerozoic Eon there have been further changes to the biological pump. In particular, a rise of eukaryotic algae from the early Jurassic onwards is hypothesised to have increased the efficiency of the biological pump and thus oxygenated shallow waters (Lu et al., 2018), but presumably deoxygenated deeper waters, at least in the short term. In the oceanic anoxic events (OAEs) that occurred during the Mesozoic Era there were major increases in prokaryotic nitrogen fixation yet evidence for a eukaryote-dominated biological pump (Higgins et al., 2012), raising interesting questions as to whether this reinforced anoxia at depth.

Previous modelling work has examined the impact of changes in the organic matter remineralisation length/depth (z_{rem}) in the 3D GENIE intermediate complexity model (Meyer et al., 2016;Lu et al., 2018). Both studies clearly demonstrated the important control of the z_{rem} on ocean oxygen concentrations – as it gets larger the oxygen minimum zone shifts to greater depths. Furthermore, Lu et al. (2018) showed that an increase in z_{rem} can explain an observed deepening of the oxycline from the Paleozoic to Meso-Cenozoic in the ocean redox proxy I/Ca. However, coarse 3D models such as GENIE do not really resolve shelf seas and their dynamics, which are distinct from those of the open ocean. Furthermore, GENIE only accounts for one organic carbon species, overlooking processes of transformation of organic material, such as coagulation and fragmentation, which contribute to modulate the efficiency of the organic matter vertical export and burial (Wilson et al., 2008;Karakaş et al., 2009;Boyd and Trull, 2007).

In this study we take a more idealised approach, exploring how changes in the properties of the biological pump may have affected the shelf sea and open ocean nutrient and redox state using a new Biological Pump, Oxygen and Phosphorus (BPOP) box model. This model combines a box representation of the marine O and P cycles with

an intermediate complexity representation of the biological pump transformations, including two classes of particulate organic matter (POM). BPOP allows us to modify the properties of two POM pools, whose abundance is regulated by the processes of production and coagulation. We focus on changes in the characteristic depths at which the two POM pools are remineralized, i.e., the particle remineralization length scale (z_{rem}), and study the resulting equilibrium budgets and fluxes. In the following sections we describe the model, we provide an evaluation of its performance in the context of modern observations and flux estimates, and finally present and discuss our model results.

2 Model description

Here we describe the Biological Pump, Oxygen and Phosphorus (BPOP) model. The model was implemented using Matlab and the equations are solved by the built-in ode15s solver. BPOP can easily run on a single core, integrating 50 million years of time in less than a minute on an ordinary machine, and is therefore computationally efficient. We refer to the user's manual (see the supplementary material) for further information on how to run the model.

2.1 Variables and circulation

The box model resolves explicitly for each relevant box the local concentrations of three types of tracers: molecular oxygen O_2 (O), inorganic dissolved phosphorus (P) and sediment organic phosphorus ($SedP_{org}$). The total budgets of P and O, respectively P^{TOT} and O^{TOT}, are also independently integrated from the net sources and sinks of the two tracers over the entire model domain, for the purpose of checking mass conservation. The entire set of the model's state and diagnostic variables and their units are listed in Table 1. In the following subsections we describe the box model's geometry and discuss the physical and geochemical fluxes that drive the tracers' dynamics. Box properties are listed in Table 2, while the set of parameters adopted for the modelled physical and geochemical fluxes can be found in Table 3.

2.1.1 Box properties and physical fluxes of inorganic tracers

The box model includes 4 ocean boxes, 1 atmospheric box and 2 sediment boxes (Figure 1a). The ocean and sediment boxes are equally split between shelf sea and open ocean, both including one surface ocean box and one deep ocean box.

O and P are exchanged between the 4 ocean boxes through advection and mixing, including an upwelling recirculation between shelf sea and open ocean (Wollast, 1998). For a generic tracer concentration C and in the i^{th} box, the physical exchange flux is represented by

$$\boldsymbol{AdvMix(C)^i = \sum_j MassFlux_{ij}/V^i \cdot (C_j - C_i)} \quad (1)$$

For each surface box *i*, air-sea gas exchange allows O fluxes between the ocean and the atmosphere (at). The flux is positive when directed into the ocean and depends on the gas transfer velocity K_w and Henry's constant K_{Henry}, as in:

$$\boldsymbol{AirSea^i = K_W \cdot (O^{at}/K_{Henry} - O^i) \cdot A^i/V^i} \quad (2)$$

where K_W is a function of the prescribed mean temperature T_{mean} and wind speed W_{speed} (Sarmiento and Gruber, 2006).

2.1.2 Initialization and boundary fluxes

The model is initialized with an even concentration of P (P_{ini}) in all the ocean boxes, zero oxygen and zero sediment P_{org}. A constant input of P from rivers (P_{in}) into the surface ocean replenishes the P ocean reservoir despite the burial flux (net sink of P_{org}) into the sediments. P_{in} is in part delivered directly to the surface open ocean (Sharples et al., 2017). At equilibrium, the P_{org} burial flux balances P_{in}. Oxidative weathering determined by atmospheric oxygen O^{at} constitutes a net sink flux for O. The weathering flux depends on a constant a baseline flux W_0 and it scales like the square root of the oxygen concentration normalised to present values $Omix_0$ (Lenton et al., 2018), following:

$$\boldsymbol{OxyWeath = W_0 \cdot \sqrt{O^{at}/Omix_0}} \quad (3)$$

2.2 Biological pump details

The modelled tracer cycles are coupled by a set of biological transformations, i.e., the biological pump, governing the cycle of production, remineralization and burial of P_{org} in the water column and in the sediments. P_{org} in the water column is resolved implicitly: at each time step all the produced P_{org} that does not reach the sediments is instantaneously remineralized. In this sense, in our model no P_{org} can accumulate in the ocean's water column. This scheme is like the one used to represent detrital POM in some modern ocean biogeochemical models (Moore et al., 2004). P and O biological fluxes are coupled by a fixed Redfield ratio OP_{Red}. The next few paragraphs describe the cycle of production, coagulation, export, remineralization and burial that constitute the biological pump representation. The full set of parameters used to resolve the P_{org} cycle is provided in Table 4.

2.2.1 Particle classes, production and coagulation

The model includes two P_{org} classes which get produced, exported and remineralized in the ocean's water column: small P_{org} (SP_{org}) and large P_{org} (LP_{org}). The use of two Porg classes is in line with modern ocean in situ observations, which reveal a bimodal distribution of the particle sizes and sinking speeds (Riley et al., 2012;Alonso-González et al., 2010). Moreover, it allows to better reproduce the commonly observed Martin power-law decay of the particle export flux with the use of a remineralization length scheme of export and burial fluxes (Boyd and Trull, 2007).

Organic matter production happens only in the surface ocean boxes through the uptake of P. This is regulated by a maximum rate P_{eff} and a Michaelis-Menten kinetics with constant K_P. Production in each i^{th} box only generates SP_{org}, according to:

$$\boldsymbol{Prod^i = P_{eff} \cdot (P^i/(P^i + K_P)) \cdot P^i} \quad (4)$$

LP_{org} is generated via the coagulation of SP_{org} either at the surface after production or at depth after the export of SP_{org} from the surface. The coagulation of SP_{org} into LP_{org} in each box *i* is proportional to the square of the local SP_{org} concentration and is regulated by a coagulation rate cg_r (Boyd and Trull, 2007;Gruber et al., 2006), as in:

$$\boldsymbol{Coag^i = cg_r \cdot (SP_{org}{}^i)^2} \quad (5)$$

Coagulation impacts the relative contribution of small and large particles to the export and burial fluxes by subtracting from the local SP_{org} pool and adding to the LP_{org} pool.

2.2.2 Physical fluxes of organic material

The implicit representation of the organic matter in the water column implies that no organic matter is accumulated in the ocean. In our baseline version of the model, corresponding to the results presented in this manuscript, SP_{org} and LP_{org} are redistributed throughout the watercolumn exclusively by implicitly modelled gravitational sinking before being either buried, accumulated in the sediments or remineralized. Even though the vertical export by downwelling and mixing (Stukel and Ducklow, 2017), and the lateral organic matter redistribution (Lovecchio et al., 2017;Inthorn et al., 2006) may be important when working with suspended SP_{org} ($z_{rem}^{S} = 0$), these fluxes are not currently accounted for in the model.

2.2.3 Remineralization length scheme

The export and sedimentation fluxes of P_{org} through the water column are represented by a remineralization length scheme. In this representation, the vertical fluxes of organic matter f(z) vary exponentially with depth. The shape of the exponential depends on the value of the remineralization length (z_{rem}) of each organic matter species:

$$\boldsymbol{f^k(z) = f_0^k \cdot e^{-\frac{z-z_0}{z_{rem}^k}}}, \quad (6)$$

where $\boldsymbol{f_0^k}$ is the flux at the reference depth $\boldsymbol{z_0}$, and the index $\boldsymbol{k}$ indicates the organic matter pool of reference, either small (S) or large (L). This representation of the export flux is convenient, as it does not depend on the specific choice of $\boldsymbol{z_0}$ (Boyd and Trull, 2007).

The remineralization length z_{rem} indicates the distance through which the particle flux becomes 1/e times (about 36 %) the flux at the reference depth (Buesseler and Boyd, 2009;Marsay et al., 2015). This quantity is expressed in metres and can be calculated as the ratio between the particle sinking speed and the particle's remineralization rate (Cavan et al., 2017). Consequently, z_{rem} implicitly contains information on several particle inherent properties (among which density, size, shape, organic matter liability) as well as information about the surrounding environment, e.g., the type of heterotrophs which feed upon the organic material (McDonnell and Buesseler, 2010;Baker et al., 2017). For simplicity, we assume that the remineralization length of small and large particles does not vary between shelf sea and open ocean boxes. We examine the potential impact of this limitation in the discussion section of the paper.

2.2.4 Sediments and burial

SPorg and LPorg accumulate in the sediments as $SedP_{org}$, which is calculated as a density per unit of area. The sediment flux into the sediment box *i* depends on the organic matter concentration in the overlaying deep ocean box *j* and on the remineralization length of the two pools as in:

$$\boldsymbol{SedFlx^i = \left(SP_{org}{}^j \cdot exp\left(-\Delta Z_j / z_{rem}^S\right) + LP_{org}{}^j \cdot exp\left(-\Delta Z_j / z_{rem}^L\right)\right) \cdot \Delta Z_j} \quad (7)$$

The accumulated $SedP_{org}$ is partially slowly remineralized and partially irreversibly buried in a mineral form. Phosphorus burial as mineral Ca-P is modelled as a function of the square of $SedP_{org}$ that accumulates in the sediments, in a way that is analogous to the dynamics of particle coagulation, and is regulated by a constant rate coefficient CaP_r. Ca-P formation happens at a lower rate under low oxygen conditions ($CaP_r^* = CaP_r \cdot fs_{an}$ with $fs_{an} < 1$), in agreement with observations and previous models (Slomp and Van Cappellen, 2006). The transition from aerobic and anaerobic conditions is controlled by a Michaelis-Menten type of function of the oxygen

concentration in the deep ocean box j overlaying the sediment box i. The oxic and anoxic terms sum to the total formation term as in:

$$\boldsymbol{CaPform^i = \left(SedP_{org}{}^i\right)^2 \cdot [CaP_r \cdot\ O^j/(O^j + K_O^s)\ +\ (CaP_r \cdot\ fs_{an})\ \cdot\ (1 -\ O^j/(O^j + K_O^s))]} \quad (8)$$

This flux is essential to balance the continuous P river input, therefore preventing the ocean from overflowing with nutrients.

2.2.5 Remineralization in the water column and sediments

At each time step, remineralization in the water column completely depletes the P_{org} that has not reached the sediments. In the two surface boxes, remineralization of P_{org} that is not exported below the euphotic layer uses up part of the oxygen that was released by production. For this reason, net oxygen production in each surface box is proportional to the export of P_{org} below the euphotic layer. Export from a surface box *i* to a deep box *j* happens both via gravitational sinking and via mixing, as in:

$$\boldsymbol{VExp^i = SP_{org}{}^i \cdot exp(-(\Delta Z_{eu}/2)\ /z_{rem}^S) + LP_{org}{}^i \cdot exp(-(\Delta Z_{eu}/2)\ /z_{rem}^L)} \quad (9)$$

At depth, the remineralization of P_{org} that does not reach the sediments happens through both aerobic and anaerobic processes, completely depleting the remaining P_{org}. Water-column remineralization of P_{org} into inorganic P in the deep box *j* is therefore calculated as:

$$\boldsymbol{WcRem^j =\ SP_{org}{}^j \cdot (1 - exp(-\Delta Z_j\ /z_{rem}^S)) + LP_{org}{}^i \cdot (1 - exp(-\Delta Z_j\ /z_{rem}^L))} \quad (10)$$

In each deep ocean box *i*, aerobic remineralization uses some of the available oxygen and is therefore limited by a Michaelis-Menten kinetics with a half-saturation constant K^w_O (DeVries and Weber, 2017). Anaerobic remineralization takes up the entire remaining P_{org} that is not remineralized aerobically and releases a product which "bubbles up" to the atmosphere, reacting with atmospheric oxygen.

In each sediment box *i*, remineralization of $SedP_{org}$ happens in a similar way to remineralization in the water column, with an aerobic and an anaerobic component. However, remineralization in the sediments is not instantaneous, but happens at a fixed rate which depends on the oxygenation state of the overlaying water column. Aerobic remineralization takes up oxygen from the overlaying deep-water box *j* and happens at a rate rm_r, while being limited by a Michaelis-Menten coefficient. Anaerobic remineralization releases its product to the atmosphere and happens at a faster rate $rm_r^* = rm_r \cdot fe_{an}$ with $fe_{an} > 1$, in agreement with recent observations and previous models (Slomp and Van Cappellen, 2006). Total sediment remineralization is therefore the sum of the two terms as in:

$$\boldsymbol{SedRem^i =\ rm_r \cdot SedP_{org}{}^i \cdot (O^j/(O^j + K_O^s))\ +\ (rm_r \cdot\ fe_{an}) \cdot SedP_{org}{}^i \cdot (1 -\ O^j/(O^j + K_O^s))} \quad (11)$$

2.3 Equations summary

The dynamics of the model's 11 state variables is regulated by just as many equations. We summarize here the major terms for P, O and $SedP_{org}$ in the surface ocean (s), deep ocean (d), atmosphere (at) and sediments, without distinguishing between coastal and open ocean boxes and assuming that all terms have been scaled with the reference box' dimensions. A full set of equations including the explicit formulation of all the flux terms for each box can be found in the paper's Appendix.

$$\frac{dP^s}{dt} = P_{in} + AdvMix(P)^s - VExp, \quad (12)$$

$$\frac{dP^d}{dt} = AdvMix(P)^d + WcRem + SedRem \quad (13)$$

$$\frac{dO^s}{dt} = AdvMix(O)^s + VExp \cdot OP_{Red} + AirSea \quad (14)$$

$$\frac{dO^d}{dt} = AdvMix(O)^d - WcRem_{Aer} \cdot OP_{Red} - SedRem_{Aer} \cdot OP_{Red} \quad (15)$$

$$\frac{dSedP_{org}}{dt} = SedFlx - CaPform - SedRem \quad (16)$$

$$\frac{dO^{at}}{dt} = -\sum AirSea - WcRem_{Ana} \cdot OP_{Red} - SedRem_{Ana} \cdot OP_{Red} - OxyWeath \quad (17)$$

Where: P_{in} is the river input of P to the ocean's surface, AdvMix indicates the advective and mixing physical fluxes of the variable of interest (which differ for each box according to the circulation scheme); Exp is the export flux of P_{org} in P units; WcRem indicates the water column complete remineralization of the organic material in P units, which is split into an anaerobic (Ana) and aerobic (Aer) component; SedRem indicates the sediment remineralization of $SedP_{org}$ in P units (also aerobic and anaerobic); AirSea represents the air-sea flux exchange of O; OxyWeath is the O weathering flux sink; SedFlx is the $SedP_{org}$ accumulation flux as regulated by the remineralization length scheme at the bottom of the water column; and finally CaPform represents the sediment burial flux of P in mineral form. For each box, flux terms are rescaled with the appropriate box geometry.

2.4 Strategy: sensitivity studies for varying z_{rem}

In order to characterize the model, we analyse the equilibrium budgets and fluxes of the state variables for varying z_{rem} values separately for SP_{org} and LP_{org}, respectively z_{rem}^S and z_{rem}^L. We adopt a range of zrem values that fall close to modern observations (Cavan et al., 2017;Buesseler and Boyd, 2009;Marsay et al., 2015) and keeps into consideration our future aim to apply the model to simulate the impact of the time evolution of the early biological pump (at the Neoproterozoic-Palaeozoic transition). For this reason, we don't push the range as far as what would be needed to consider the impact of fast sinking rates typical of silicified or calcified small phytoplankton (McDonnell and Buesseler, 2010;Lam et al., 2011). In our sensitivity simulations, z_{rem}^S is in the range of [0, 40 m], while z_{rem}^L varies in the range of [50 m, 450 m].

3 Evaluation

3.1 Timescales

Starting from the initial values listed in Table 3, the modelled state variables evolve towards equilibrium for any couple of values of z_{rem}^S and z_{rem}^L in the explored interval. Simple mass conservation checks show no hidden source or sink of tracers in the model's boxes. Figure 3 illustrates an example of evolution of the variables for z_{rem}^S and z_{rem}^L in the middle of the interval of explored values for both particle types. In all the ocean boxes, P shows an initial oscillation that evolves on timescales of tens of thousands of years (Figure 3a,b), as expected by the typical timescale of evolution of the tracer (Lenton and Watson, 2000). This is followed by a slower drift which depends on the dynamics of the deep water oxygen content, as the release and burial of P in the sediments depends on the level of oxygenation of the deep ocean and especially of the deep shelf sea. P reaches complete

equilibrium as soon as the deep ocean boxes become stably oxygenated. The timescales of evolution of O are slower and lay on the order of tens of millions of years (Lenton and Watson, 2000). Oxygen in the deep shelf overcomes hypoxia after the first few millions of years and then slowly evolves towards equilibrium on the same timescale of O in the other ocean boxes. The dynamics of SedPorg is also strongly driven by level of oxygenation of the deep shelf sea.

3.2 Modern ocean budgets and fluxes

Modern estimates of the z_{rem}^S and z_{rem}^L vary depending on the region of sampling and on the local community structure, with most of the measurements focusing on large or heavy particles and most studies focusing on the open ocean (Iversen and Ploug, 2010;Cavan et al., 2017;Lam et al., 2011). Furthermore, only a very limited number of measurements accounts for both microbial and zooplankton remineralization, the latter disregarded by lab measurements of z_{rem} (Cavan et al., 2017). Considering the fundamental role of the shelf sea in our model (always accounting for > 98 % of the total burial), we evaluate modelled tracer budgets and fluxes for values of z_{rem}^L that lay around 76 m, as measured in situ by Cavan et al. (2017) for a modern shelf sea. We pose no restrictions on z_{rem}^S due to the lack of precise measurements. A summary of our evaluation is provided in Table 5.

In the above mentioned range of z_{rem}, our model predicts equilibrium budgets of between 3200 TmolP and 3400 TmolP for phosphorus, and an oxygen budget of between 100 $PmolO_2$ and 150 $PmolO_2$ in the entire ocean, compared to the estimated total P reservoir of 3100 TmolP (Watson et al., 2017) and estimated deep ocean O_2 reservoir of 220 $PmolO_2$ (Slomp and Van Cappellen, 2006). Due to the relative size of the ocean boxes, it is important to underline that total budgets are strongly driven by the deep open ocean budget.

Deep shelf P and O concentrations lay in the ranges of [4.5 mmol m^{-3}, 6 mmol m^{-3}] and [4 mmol m^{-3}, 20 mmol m^{-3}] respectively (Figure 5,6). Deep shelf nutrient concentrations are higher than expected by a factor of two or three compared to modern values, possibly due to the fact that our model does not store any P_{org} in the water column or due to an underestimation of the vertical supply of nutrients to the surface shelf (e.g., via mixing). Limiting deep P concentrations via lower remineralization or higher burial rates, however, also results in sensibly lower production rates. In the deep open ocean, P and O concentrations fall in the ranges of [2.7 mmol m^{-3}, 3 mmol m^{-3}] and [75 mmol m^{-3}, 125 mmol m^{-3}] respectively. For any combination of z_{rem}^S and z_{rem}^L, O levels in surface ocean boxes lay between 273 mmol m^{-3} and 272.5 mmol m^{-3}, a good approximation of average modern surface values (Garcia et al., 2018a). In general, the deep shelf always shows the highest P values and lowest O concentrations compared to the other ocean regions, while, as expected, the surface shelf sea is richer in P compared to the surface open ocean.

Modelled biological fluxes, such as production and export, fall around the low end of present estimates (Figure 7). Our model predicts an equivalent C primary production of between 1400 TmolC yr^{-1} and 3000 TmolC yr^{-1}, and an export below the euphotic layer ranges between 300 TmolC yr^{-1} and 430 TmolC yr^{-1}, both calculated using a fixed C:P Redfield ratio of 106. These must be compared to an expected value of production of at least 3300 TmolC yr^{-1} (Carr et al., 2006) and an estimated export flux of at least 415 TmolC yr^{-1} (Henson et al., 2011). Despite the absolute fluxes being lower than expected, modelled export production (the export to production ratio) and the burial to production ratio compare well to range of present estimates. The modelled export corresponds to between 10 % and 32 % of total production, strongly depending on z_{rem}^S, compared to an expected range of 2 % -

20 % (Boyd and Trull, 2007). Buried P_{org} corresponds to between 0.3 % and 0.7 % of total production, compared to an expected 0.4 % (Sarmiento and Gruber, 2006).

In terms of the shelf contribution to the total fluxes, model results also fall close to present estimates. Modelled production in the surface shelf sea represents between 12% and 20% of total production (expected 20%) (Barrón and Duarte, 2015;Wollast, 1998). The fraction of modelled export and burial that happens in the shelf region represent, respectively, [20 %, 23 %] and nearly 100 % of the total ocean fluxes, compared to estimated modern values of 29 % and 91 % (Sarmiento and Gruber, 2006). Our overestimation of the shelf contribution to the burial fluxes may be due to the underestimation of the open ocean particles z_{rem} compared to observations (Cavan et al., 2017;Lam et al., 2011), i.e. our choice of using the same value of z_{rem}^S and z_{rem}^L for both the coastal and the open ocean box. This simplifying assumption limits the capacity of P_{org} to reach the deep sediment layer in the open ocean. We explore potential limitations of this choice in the Discussion section.

4 Results

4.1 Budgets and fluxes sensitivity to changes in z_{rem}

Around the lowest values of z_{rem}^L adopted in the present study, i.e., in the range of [50 m, 100 m], our model shows a strong sensitivity of the total and local ocean P and O budgets for small changes of z_{rem}^L (Figure 4). This is true for any z_{rem}^S, with minor differences between low and high z_{rem}^S values. For smaller z_{rem}^L, the model shows a sharp increase in P concentrations in all the ocean boxes and a substantial decrease of O levels at depth (Figures 5,6), which are coupled to high levels of production and remineralization and low rates of sedimentation (Figure 7). Essentially slow sinking and/or rapid remineralization results in inefficient removal of P to shelf sea sediments, requiring the ocean concentration of P to rise considerably for P output to balance (fixed) P input to the ocean.

Our model results show that for any couple of values of z_{rem}^S and z_{rem}^L in the entire explored range, the biological pump is able to oxygenate the surface ocean (surface O levels lay close to 273 mmol m^{-3}) and, for most values, also to maintain the deep ocean above the level of hypoxia (Figure 6). The model shows a substantial difference between the deep shelf and the deep open ocean: while the latter is substantially oxygenated (O > 50 mmol m^{-3}) for nearly any value of z_{rem}^S and z_{rem}^L, the deep shelf is hypoxic or even suboxic for a broad range of small values of z_{rem}^L, especially close to modern shelf z_{rem}^L observations. Considering the wide spatial extension of our boxes, we expect these low oxygen levels to indicate the development of local anoxia in the deep shelf.

In a limited interval of small z_{rem}^S values (roughly $z_{rem}^S < 6$ m), model results depend only on the LP_{org} properties due to the rather irrelevant contribution of SP_{org} to export and remineralization. For larger z_{rem} values ($z_{rem}^S > 6$ m and $z_{rem}^L > 100$ m), model results show a strong interdependence of equilibrium budgets and absolute fluxes on both z_{rem}^S and z_{rem}^L. Interestingly, in this range of values, export production depends nearly entirely on the small particle properties, ranging between 10 % for low z_{rem}^S and 32 % for high z_{rem}^S, an overall trend that affects also the ratio of deep remineralization to surface production (Figure 7).

It is also important to notice that, for any couple of z_{rem}^S and z_{rem}^L, modelled tracer concentrations and fluxes fall in a range of values that never exceeds by orders of magnitude the modern observed values. Considering all of the ocean boxes, P concentrations vary in the range of roughly 0.3 mmol m^{-3} and 8 mmol m^{-3}, while O levels lay between 1 mmol m^{-3} and 200 mmol m^{-3}. Production in carbon units lays in the interval [800 TmolC yr^{-1}, 4100 TmolC yr^{-1}].

4.2 Budgets and fluxes contribution by particle class

The relative role of small and large particles to modelled biological and physical fluxes depends on a combination of their inherent properties (z_{rem}) and of coagulation. Coagulation of SP_{org} into LP_{org} after production in surface boxes affects between 13 % and 55 % of the small particles in the surface shelf sea and between 4 % and 28 % of the small particles in the surface open ocean (Figure 8a,b). The highest rates of coagulation of SP_{org} into LP_{org} in the surface ocean are found for especially high P concentrations resulting in high rates of small particle production. Rates decrease quickly moving away from these high P condition. These correspond to roughly $z_{rem}^{L} < 100$ m, meaning rather labile or light large particles, which contribute poorly to P removal and net O production.

For $z_{rem}^{L} > 100$ m, LP_{org} efficiently remove P from the water column, limiting production. Coagulation rates are therefore lower and vary in a more limited range of values. For this reason, the contribution of SP_{org} to the total export below the euphotic layer is strongly dominated by the value of z_{rem}^{S}, with a null contribution to export for all values of $z_{rem}^{S} < 10$ m and increasing values above it. This trend is reflected in the deep-water small particle fraction (Figure 8c,d). Coagulation rates at depth, even though lower compared to the surface, still reach values of a few percent in the shelf sea (≤ 6 % of the exported SP_{org}). Small particles contribute up to 66 % to export and up to 25 % to the sediment accumulation in the shelf sea, with the highest contribution to sediment accumulation being reached for large z_{rem}^{S} and low z_{rem}^{L}. In the open ocean, small particles represent up to 87 % of the total export, with the percentage being strongly dependent on the value of z_{rem}^{S}. Our model highlights therefore the different role of large and small particles in the determination of the equilibrium budgets and fluxes. Coagulation into large (fast sinking, less liable) particles is essential to maintain high enough sedimentation and burial rates, therefore allowing O accumulation in the system. At the same time, small (slow sinking, more liable) particles tune the total magnitude of export and remineralization below the euphotic layer, impacting the distribution of oxygen and nutrients throughout the water column.

5 Discussion

5.1 Model limitations and robustness

5.1.1 Box model limitations

BPOP consists in a simple box model with 4 ocean boxes, 2 sediment boxes and 1 atmospheric box. As with every box model, BPOP only allows a very rough and fundamental representation of the ocean's topography and circulation as well as of the exchange fluxes between ocean, atmosphere and sediments. Even though this may be a limitation in the context of the study of the well-known modern (and future) ocean, such a computationally inexpensive model can be a useful tool to for a first exploration of a large variety of projected conditions. In the context of understanding past ocean changes, often characterized by a limited availability of observational data, the use of such a simple model constitutes instead an effective and honest approach to understand global shifts in budgets and fluxes. Furthermore, BPOP explicitly distinguishes between the well sampled shelf sea and the less known open ocean of deep time, therefore allowing to relate shelf data with large scale open sea conditions.

5.1.2 Limitations connected to the biological pump representation

In our model we adopt a very simplified representation of the biological pump, including two particle classes, "small" and "large", generated by production and coagulation, assuming that, on average, $z_{rem}^S < z_{rem}^L$. This scheme resembles the one commonly used in ocean biogeochemical models (Gruber et al., 2006;Jackson and Burd, 2015). Our model does not include a DOM pool for reasons mostly connected to the implicit representation of the biological pump and the complete remineralization of the non-sedimented organic material at each integration step.

Modelled particles get remineralized through the water column according to their characteristic z_{rem}. Even though for simplicity we do not use a continuum spectrum of z_{rem}, the use of two particles classes is in line with observations showing two distinct peaks in the observed distribution of particles' sinking speeds (Riley et al., 2012;Alonso-González et al., 2010). Furthermore, this simplification still allows to closely approximate the empirical particle flux curve as a function of depth, also known as Martin's curve (Boyd and Trull, 2007).

We assume that z_{rem}^S and z_{rem}^L do not vary between the shelf sea and the open ocean. However, modern ocean observations show cross-shore changes in the phytoplankton community structure and sinking speeds (Barton et al., 2013). Our simplifying assumption may therefore cause the overestimation of the relative contribution of the shelf sea to the total burial flux of P_{org}. Despite this, we believe that this choice is still convenient in the context of the current model, as it allows us to reduce the number of parameters in such a simple box model representation of the ocean's biological pump.

Observations suggest that hard shelled phytoplankton types, especially calcified cells, contribute substantially to the vertical export and burial of the organic material thanks to extremely large z_{rem} despite their small size (Lam et al., 2011;Iversen and Ploug, 2010). In the present study we focus on an interval of z_{rem}^S and z_{rem}^L values that are most likely to resemble the biological pump conditions of the Neoproterozoic - early Paleozoic ocean, before the evolution of such phytoplankton types. However, the model allows to explore different ranges of z_{rem}^S and z_{rem}^L values and to tune the rate of coagulation in order to explore the influence of these phytoplankton classes.

Even though bacterial remineralization is thought to be the dominant pathway for organic matter recycling on a global scale, especially at low latitudes (Rivkin and Legendre, 2001), modern ocean coastal environments are also characterized by high grazing rates. The evolution of zooplankton and increasingly large grazers may have had a different impact on the effective z_{rem}^S and low z_{rem}^L, given additional P_{org} transformations such as particle fragmentation due to sloppy feeding (Cavan et al., 2017;Iversen and Poulsen, 2007). These processes can limit the large particle burial rates, while resulting in the deep production of small particle, s-POM and DOM. Our model does not currently account for particle fragmentation, however the process could be easily considered in future model developments. In this context, new processes such as the sedimentation and burial of large grazers should also be considered.

5.1.3 Sensitivity to parameter choices

We discuss here the model sensitivity to changes in a set of significant parameters adopted to describe its geometry, circulation and biological processes. Overall, none of the sensitivity experiments showed significant changes in the model results and conclusions: trends in budgets and fluxes obtained varying z_{rem}^S and z_{rem}^L, as well as our main results regarding the relative deep shelf and open ocean oxygenation remain unchanged.

Among the geometrical box model parameters, a key value is represented by the percentage of shelf sea area ($\mathcal{P}_{shelf}$). An increase (e.g., doubling) in $\mathcal{P}_{shelf}$ results in an overall decrease in the total budget of P and increase in O due to the larger ratio of burial to production, which is facilitated by a larger extension of the surface of shallow water. Interestingly, deep shelf anoxia is enhanced for larger $\mathcal{P}_{shelf}$, i.e., anoxia is observed for a wider range of z_{rem}^{S} and z_{rem}^{L} values, while the deep ocean tends to be more oxygenated. Despite a doubling of $\mathcal{P}_{shelf}$, however, model results largely remain in the same range of those found for modern $\mathcal{P}_{shelf}$.

We explored the effect of varying the physical circulation parameters. Changes in upwelling (Upw), have an important impact on the modelled ocean's budgets. An increase in Upw induces a lowering of P levels, especially in the deep shelf, due to their recirculation towards the surface and consequent uptake by production. This is coupled to an overall larger equilibrium O budget due to higher storage in the deep open ocean, and consequent recirculation into the deep shelf. Deep shelf suboxia is still possible, but for a more limited range of z_{rem}^{L} values. Changes in vertical mixing in the open ocean (Mix_{vo}) affect the overall P and O budgets mostly for high z_{rem}^{L}. For lower Mix_{vo}, the O budget decreases due to lower O storage at depth, while P increases. Changes in vertical mixing on the shelf (Mix_{vs}), instead, have a minor impact on the model's total budgets and fluxes, while locally modulating shelf oxygen and nutrient concentrations. Lateral mixing fluxes (Mix_{ls}, Mix_{ld}) were included in our model for means of generalization and in order to account for the influence of non-upwelling margins, with a lower value than in previous studies (Fennel et al., 2005). Changes in Mix_{ls} and Mix_{ld} result in significant changes in the deep ocean storage of tracers and on open ocean production, with little impact on the budget of the other ocean boxes. However, also in this case, our main conclusions remain unaffected.

We explored the impact of changing the portion of nutrients delivered directly to the open ocean, $\mathcal{P}_{open}$. Even large changes in this parameter do not significantly affect the model's results, indicating that the relative levels of P and O at equilibrium are determined by the internal physical and biogeochemical dynamics of the model, rather than by boundary conditions.

Lastly, we explored the model sensitivity to the choice of key biogeochemical parameters representing rates of transformation. Both the use of higher coagulation rates (cg_r) and the use of higher rates of formation of mineral Ca-P (CaP_r) result in a general increase in O levels and decrease in nutrient availability due to larger sedimentation and burial rates. However, we find again no substantial change in the model behaviour nor in the relative contribution to budgets and fluxes of each modelled ocean box.

5.2 Model applications

5.2.1 Past changes in the biological pump

The evolution of larger and heavier cells during the Neoproterozoic and across the Neoproterozoic-Paleozoic transition is hypothesised to have caused significant changes in the ocean's nutrient and redox state (Lenton and Daines, 2018). Our new model can be used to assess the impact of this evolution in both the shelf and the open ocean. Our first model results highlight that for small z_{rem}^{L}, i.e., for an early biological pump with reduced capacity of export and burial, nutrient levels and production rates are particularly high. At the same time, an increase in z_{rem}^{S} alone, fuelling higher remineralization rates at depth, can induce anoxia in the deep shelf while still maintaining the deep open ocean substantially oxygenated. The possibility of a coexistence of an anoxic deep shelf with an oxygenated deep open ocean has important implications for the interpretation of deep time redox proxy data, which come almost exclusively from shelf and slope environments, yet have been widely used to infer

deep ocean anoxia for most of the Proterozoic Eon (Lenton and Daines, 2017) . We plan to use our model to further explore these changes in a time-frame perspective, introducing time varying boundary conditions (such as changes in P_{in}) and parameter properties.

Phytoplankton evolution as well as the development of heavier and larger marine organisms continued throughout the Phanerozoic (Katz et al., 2007). BPOP can also be used to explore the role of the biological pump in the onset of OAEs in the course of the Mesozoic era, likely induced by enhanced productivity due to an upwelling intensification (Higgins et al., 2012). During the Mesozoic era, the evolution of dinoflagellates, calcareous and silica-encased phytoplankton also likely impacted the export and burial rates in a significant way (Katz et al., 2004). By extending the range of explored values of z_{rem}^{S} and z_{rem}^{L}, or possibly including the effect of grazing and/or an additional heavy POC class for shelled organisms, BPOP can also be used to study the consequences of such evolution.

5.2.2 Future changes in the biological pump

Predicted future changes connected to global warming include, among the others, changes in ocean temperature, pH and stratification (Gruber et al., 2004), with additional repercussions on plankton community structure, production, remineralization and export rates (Laufkötter et al., 2017;Acevedo-Trejos et al., 2014;Kwon et al., 2009). Our results show that around values of z_{rem}^{L} measured for modern shelf environment (Cavan et al., 2017) modelled equilibrium budgets and fluxes are very sensitive to small changes in z_{rem}. This indicates a potentially high sensitivity of the modern ocean to small changes in the biological pump, which may be particularly important in the deep shelf, where the boundary with suboxia is especially close (Keeling et al., 2010). Our model can be used to get a first assessment of the large-scale combined effect of predicted changes in the biological pump with expected shifts in the physical ocean properties.

5.2.3 Exploring past and future changes in geometry, physics and biogeochemistry

In the present study we have focused on the impact of changes of z_{rem}^{S} and z_{rem}^{L} on the equilibrium budget and fluxes in the ocean. However, BPOP can be used to explore the effect of global changes in other physical or biogeochemical processes coupled to the biological pump dynamics. Aside from testing the robustness of our results, the sensitivity tests presented in subsection 5.1.3 serve also as a first exploration of the possibility to apply the model to these further studies. We discuss here a few examples of past changes that could be explored with the present model.

Through Earth's history, variations in the distribution of continents and in the mean sea level height likely impacted the percentage of shelf sea area ($\mathcal{P}_{shelf}$) throughout the global ocean (Katz et al., 2007). Changes in climate and therefore in the mean temperature are expected to have affected both the air-sea gas exchange of oxygen (Schmidt number, $N_{Sch}(T_{mean})$) and vertical mixing (Mix_{vo}) (Petit et al., 1999). Reduced vertical mixing in warm periods is also expected to be relevant in the future because of global warming (Gruber et al., 2004). Changes in temperature are also known to impact biological activity directly, e.g,, by increasing remineralization rates (rm_r) (Laufkötter et al., 2017), and indirectly, e.g., affecting production and mortality rates through changes in the mixed layer depth (Polovina et al., 1995). Lastly, climatic shifts can also cause changes in the intensity of alongshore winds and therefore in the upwelling circulation (Sydeman et al., 2014).

6 Conclusions and Outlook

This paper provides a description, evaluation and discussion of the new BPOP model. BPOP is aimed at exploring the effects of changes in the biological pump on the shelf and open ocean nutrient and redox state as well as on P and O fluxes. This model can be adopted for a large variety of studies aimed at exploring the impact of changes in the biological pump, i.e., the particle remineralization length scale z_{rem}, in past and future ocean settings. Furthermore, it allows to couple changes in POM properties to changes in the ocean's geometry, circulation and boundary conditions.

Despite its simple representation of the ocean circulation and of the biological pump, the model can reasonably simulate values of the current P and O tracer budgets and biological pump fluxes. The model predicts potentially large variations in these P and O budgets and fluxes for past and future changes in the POM remineralization length. Our preliminary results also indicate that the early ocean may have been nutrient rich, with high levels of production and remineralization and that an anoxic deep shelf setting may have been compatible with an oxygenated deep open ocean.

We plan to apply this model to study the time evolution of the P and O budgets in both the shelf and the open ocean environment across the Neoproterozoic-Phanerozoic transition. Further developments of the model will be aimed at accounting for successive evolutionary innovations, including particle fragmentation due to grazing.

Code availability

The code is available for download in the supplementary material of the present publication, which also includes the user's manual.

Author contributions

TL and EL conceived the study. EL conceived and implemented the model. EL and TL evaluated and improved the model. Both authors contributed to the interpretation of the results, and to the writing of the present manuscript.

Competing interests

The authors declare that they have no conflict of interest.

Name	Description	Units
P^{ss}	Inorganic phosphorus in surface shelf sea box	mmol m^{-3}
P^{ds}	Inorganic phosphorus in deep shelf sea box	mmol m^{-3}
P^{so}	Inorganic phosphorus in surface open ocean box	mmol m^{-3}
P^{do}	Inorganic phosphorus in deep open ocean box	mmol m^{-3}
O^{ss}	Molecular oxygen in surface shelf box	mmol m^{-3}
O^{ds}	Molecular oxygen in deep shelf box	mmol m^{-3}
O^{so}	Molecular oxygen in surface open ocean box	mmol m^{-3}
O^{do}	Molecular oxygen in deep open ocean box	mmol m^{-3}
O^{at}	Oxygen mixing ratio in atmosphere (mol mol^{-1})	-
$SedP_{org}^{s}$	Organic phosphorus in the sediments of the shelf sea	mmol m^{-2}
$SedP_{org}^{o}$	Organic phosphorus in the sediments of the open ocean	mmol m^{-2}
P^{TOT}	Diagnostic variable: total P budget from sources and sinks only	Tmol P
O^{TOT}	Diagnostic variable: total O budget from sources and sinks only	Pmol O_2

Table 1: List of the model's state variables and of their units

Name	Description	Value	Units	Source
Mol_{atmo}	Millimoles of air in atmospheric box	$1.8 \cdot 10^{23}$	mmol	-
ΔZ_{eu}	Depth of the euphotic layer in shelf and open ocean	100	m	[1]
ΔZ_{ds}	Depth of the deep shelf sea box	100	m	[2]
ΔZ_{do}	Depth of the deep open ocean box	3500	m	[3]
A_{ocean}	Total area covered by the ocean	$361 \cdot 10^{12}$	m^2	-
$\mathcal{P}_{shelf}$	Fraction of the total ocean area currently covered by the shelf sea (≤ 200 m deep)	0.07	-	Barrón and Duarte (2015)

Table 2: Parameters set that describes the box model's geometry: [1] we assume a constant average euphotic layer depth of 100 m in both shelf and open sea; [2] the shelf sea is assumed to be 200 m deep in total, in line with the definition of shelf sea by Barrón and Duarte (2015); [3] we assume an average open ocean depth of 3600 m (including euphotic layer).

Name	Description	Value	Units	Source
P_{ini}	Initial P concentration for all the ocean boxes	2.2	mmol m^{-3}	Watson et al. (2017)
O_{ini}	Initial O concentration for all the ocean & atmosphere boxes	0	mmol m^{-3}	-
$(P_{org})_{ini}$	Initial P_{org} in all the sediment boxes	0	mmol m^{-3}	-
Upw	Upwelling cell mass fluxes	5.5	Sv	Chavez and Messié (2009)
Mix_{vo}	Vertical mixing in the open ocean	40	Sv	[1]
Mix_{ls}	Lateral mixing at the surface	1.5	Sv	[2]
Mix_{ld}	Lateral mixing at depth	1.5	Sv	[2]
Mix_{vs}	Vertical mixing in the shelf sea	1	Sv	[3]
spy	Seconds per year conversion factor (Sv to m^3 yr^{-1})	31557600	s yr^{-1}	-
P_{in}	Total P river input	$92 \cdot 10^{12}$	mmol yr^{-1}	Slomp and Van Cappellen (2006)
$\mathcal{P}_{open}$	Fraction of river input delivered to the open ocean	0.4	-	[4]
OP_{Red}	Oxygen to phosphorus Redfield ratio	106	-	[5]
T_{mean}	Global mean temperature for oxygen's Schmidt number	17.64	^oC	Sarmiento and Gruber (2006)
W_{speed}	Global mean wind speed for oxygen gas transfer velocity	7.5	m/s	Sarmiento and Gruber (2006)
T_{mean}	Global mean temperature for oxygen gas transfer velocity	17.64	^oC	Sarmiento and Gruber (2006)
K_{Henri}	Henry's law constant	$770 \cdot 10^{-6}$	m^3 atm $mmol^{-1}$	-
$Omix_0$	Today's oxygen mixing ratio in atmosphere	0.21	-	-
W_0	Baseline oxidative weathering flux coefficient	$9.752 \cdot 10^{15}$	mmol yr^{-1}	[6]

Table 3: Parameters set pertaining to the model's initial conditions, circulation mass fluxes, boundary fluxes. Notes: [1] compare to: 38 Sv (Sarmiento and Gruber, 2006), 17 Sv of mixing flux in the Southern Ocean alone (Meyer et al., 2015), estimated open ocean downwelling 38.5 Sv and upwelling 34.5 Sv (Ganachaud and Wunsch, 2000); [2] cross-shelf mass exchange due to lateral recirculation, tides and mixing aimed at including exchange processes other than upwelling (Fennel et al., 2005;Cole et al., 2015;Wollast, 1998); [3] minimal assumption for vertical mixing in nearshore regions due to seasonal and eddy mixing, see also subsection 3.2 Sensitivity to parameter choices; [4] up to 70% of river outflow reaches the open ocean, see Sharples et al. (2017); [5] assuming a constant 1:1=C:O_2 ratio and a Redfield ratio of C:P=106; [6] calculated from the equilibrium solution given P_{in}.

Name	Description	Value	Units	Source
P_{eff}	P maximum uptake rate for production	0.8	yr^{-1}	[1]
K_P	Michaelis Menten constant for P uptake	0.2	mmol m^{-3}	[2]
K^s_O	Michaelis Menten constant for aerobic remineralization in the sediments	0.2	mmol m^{-3}	[3]
K^w_O	Michaelis Menten constant for aerobic remineralization in the watercolumn	15	mmol m^{-3}	[4]
cg_r	Coagulation rate of small Porg into large Porg	0. 24	(mmol m^{-3}) $^{-1}$ yr^{-1}	[5]
rm_r	Remineralization rate of sedimented Porg	0.73	yr^{-1}	[5]
fe_{an}	Remineralization enhancement factor under anoxia	1.25	-	Slomp and Van Cappellen (2006)
CaP_r	Rate of formation of Ca-P mineral from sedimented Porg	0.4	(mmol m^{-2}) $^{-1}$ yr^{-1}	[6]
fs_{an}	Ca-P formation dampening factor under anoxia	0.5	-	Slomp and Van Cappellen (2006)

Table 4: Parameters set pertaining to the model's Porg cycle and coupled biogeochemical fluxes: [1] maximum P uptake rate, meant to account for environmental limitations of phytoplankton growth rate (such as light and temperature), the magnitude of the rate keeps into account that we are not explicitly resolving phytoplankton concentrations (order of 10^{-2} mmolP m^{-3}), see also production in Gruber et al. (2006) and Yool & Tyrrell (2003); [2] measured values vary in the range of 0.01 mmol m^{-3} up to a few mmol m^{-3}, varying for different phytoplankton types, see Lomas et al. (2014), Tantanasarit et al. (2013), Krumhardt et al. (2013), Lin et al. (2016), Klausmeier et al. (2004); [3] measured half-saturation constant for oxygen uptake varies in the range of 0.1 - 3 mmol m^{-3} (Ploug, 2001); [4] biogeochemical models commonly switch to anaerobic respiration below 4 mmol m^{-3} (Paulmier et al., 2009), measurements suggest a value close to 19 mmol m^{-3} (DeVries and Weber, 2017); [5] on the same order of magnitude as Gruber et al. (2006); [5] unmeasured – given the analogous adopted functional form, we assume Ca-P formation to happen on a timescale close to that of P_{org} coagulation in the water column.

Quantity	Model	Modern values or estimates	Units	Source
Total ocean P	3200 - 3400	3100	TmolP	Watson et al. (2017)
Total ocean O_2	100 - 150	220 (deep ocean)	PmolO_2	Slomp and Van Cappellen (2006)
P^{ss}	1.5 – 1.8	1 – 1.5	mmol m^{-3}	Garcia et al. (2018b);Sarmiento and Gruber (2006)
P^{ds}	4.5 – 6	2.2	mmol m^{-3}	Garcia et al. (2018b);Watson et al. (2017)
P^{so}	0.5 - 1	0.2 - 2	mmol m^{-3}	Garcia et al. (2018b);Sarmiento and Gruber (2006)
P^{do}	2.7 - 3	1 - 3	mmol m^{-3}	Garcia et al. (2018b);Sarmiento and Gruber (2006)
O^{ss}	273	200 - 350	mmol m^{-3}	Garcia et al. (2018a)
O^{ds}	4 - 20	0-80	mmol m^{-3}	Garcia et al. (2018a)
O^{so}	273	200 - 350	mmol m^{-3}	Garcia et al. (2018a)
O^{do}	75 - 120	40-200	mmol m^{-3}	Garcia et al. (2018a)
Production (Prod)	1400 - 3000	3300 - 9000	TmolC yr^{-1}	Carr et al. (2006)
Export	300 - 430	415 – 1660	TmolC yr^{-1}	Henson et al. (2011)
Export production	10 % - 32 %	2 % - 20 %	of total Prod	Boyd and Trull (2007)
Burial	0.3 % - 0.7 %	0.4 %	of total Prod	Sarmiento and Gruber (2006)
Shelf sea production	12 % - 20 %	20 %	of total Prod	Barrón and Duarte (2015);Wollast (1998)
Shelf sea export	20 % - 23 %	29 %	of total Export	Sarmiento and Gruber (2006)
Shelf sea burial	100 %	91 %	of total Burial	Sarmiento and Gruber (2006)

Table 5: Summary of the model evaluation provided in section 3. Modern observations and estimates are compared to model results obtained for z_{rem}^{L} in the range of measured values for a modern shelf sea (Cavan et al., 2017).

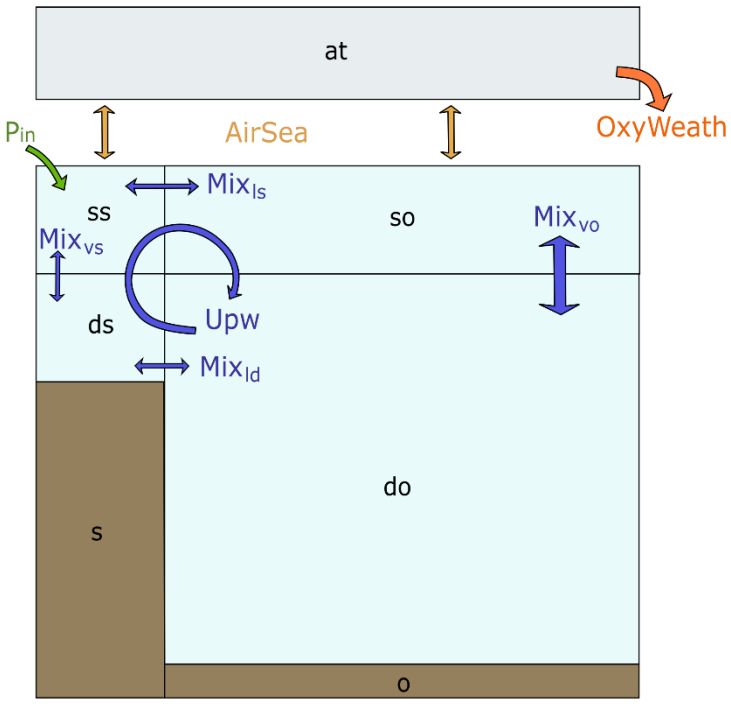

Figure 1: Box model scheme with a representation of the physical and boundary fluxes affecting inorganic tracers in the water column and atmosphere, where blue arrows indicate advective and mixing fluxes and yellow arrows indicate air/sea gas exchange fluxes. The model includes 7 boxes: surface shelf (ss), deep shelf (ds), surface open ocean (so), deep open ocean (do), atmosphere (at), shelf sediments (s), open ocean sediments (o).

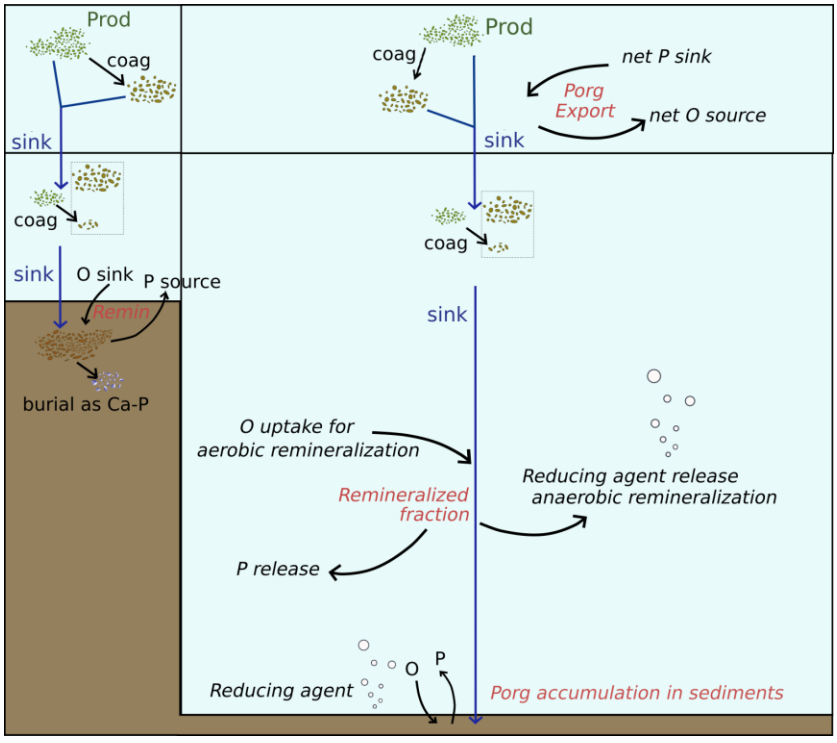

Figure 2: Representation of the physical and biogeochemical fluxes affecting the P_{org} cycling in the model. Even though some processes (such as burial as Ca-P) are here represented in detail only in one box, the set of biogeochemical processes regulating the P_{org} dynamics in shelf sea and open ocean (both water column and sediments) is the same, as described in subsection 2.2.

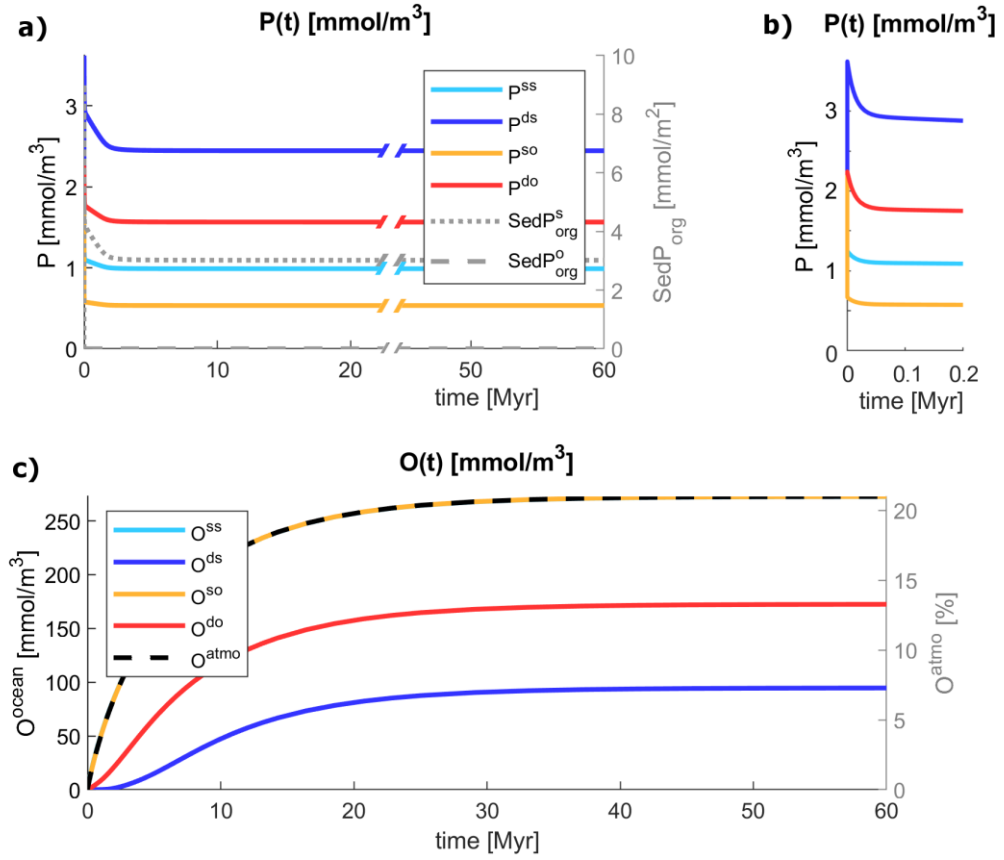

Figure 3: Evolution of the state variables from the initial conditions listed in Table 2 and remineralization lengths roughly in the middle of the interval of explored values: z_{rem}^S = 20 m, z_{rem}^L = 250 m. (a) Evolution of inorganic phosphorus P in the water column (left axis) and of organic phosphorus in the sediments $SedP_{org}$ (right axis); (b) zoom on the dynamics of P in the two hundred thousand years; (c) Evolution of oxygen in the water column (left axis) and atmosphere (right axis). In subplot (c) the two lines O^{ss} and O^{so} are overlapping: the two variables evolve closely due to the couplingof the surface ocean with the atmosphere via air-sea gas exchange.

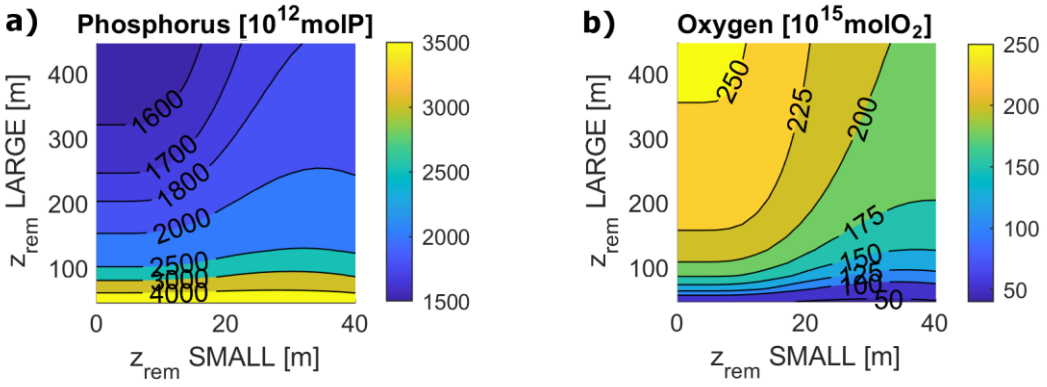

Figure 4: Total ocean budgets of (a) P and (b) O at equilibrium for varying z_{rem}^S and z_{rem}^L.

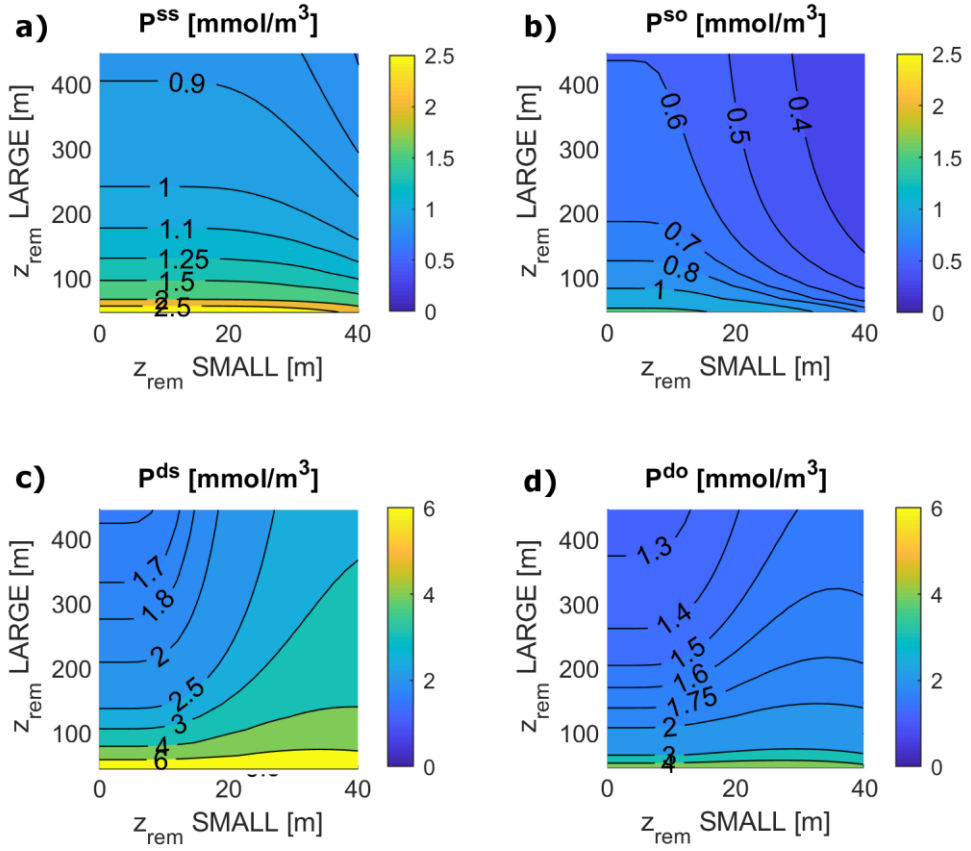

Figure 5: Local P concentration in each ocean box for varying z_{rem}^S and z_{rem}^L: (a) surface shelf sea, ss; (b) surface open ocean, so; (c) deep shelf sea, ds; (d) deep open ocean, do. Surface ocean boxes, as well as deep ocean boxes, are plotted on the same scale.

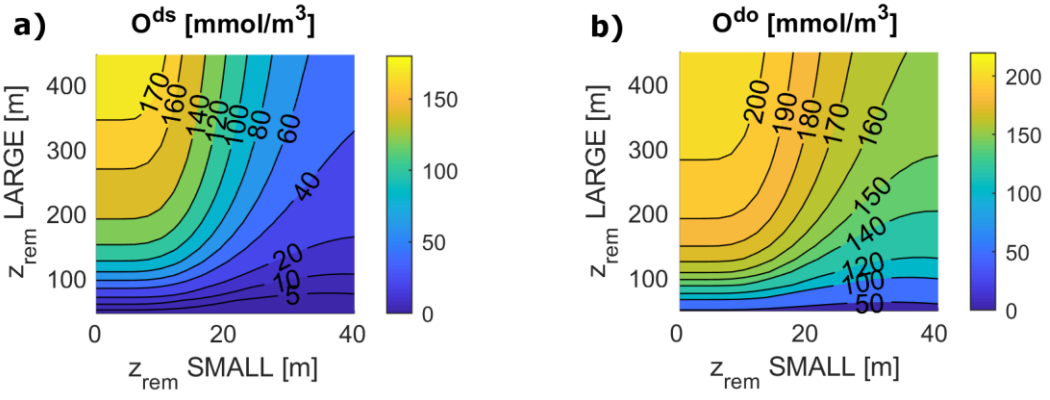

Figure 6: O concentrations at equilibrium for varying z_{rem}^S and z_{rem}^L: (a) deep shelf sea, ds; (b) deep open ocean, do. Surface ocean boxes (not shown) have nearly constant values of O for any set of z_{rem} due to the air-sea gas exchange, which strongly couples them to the atmosphere.

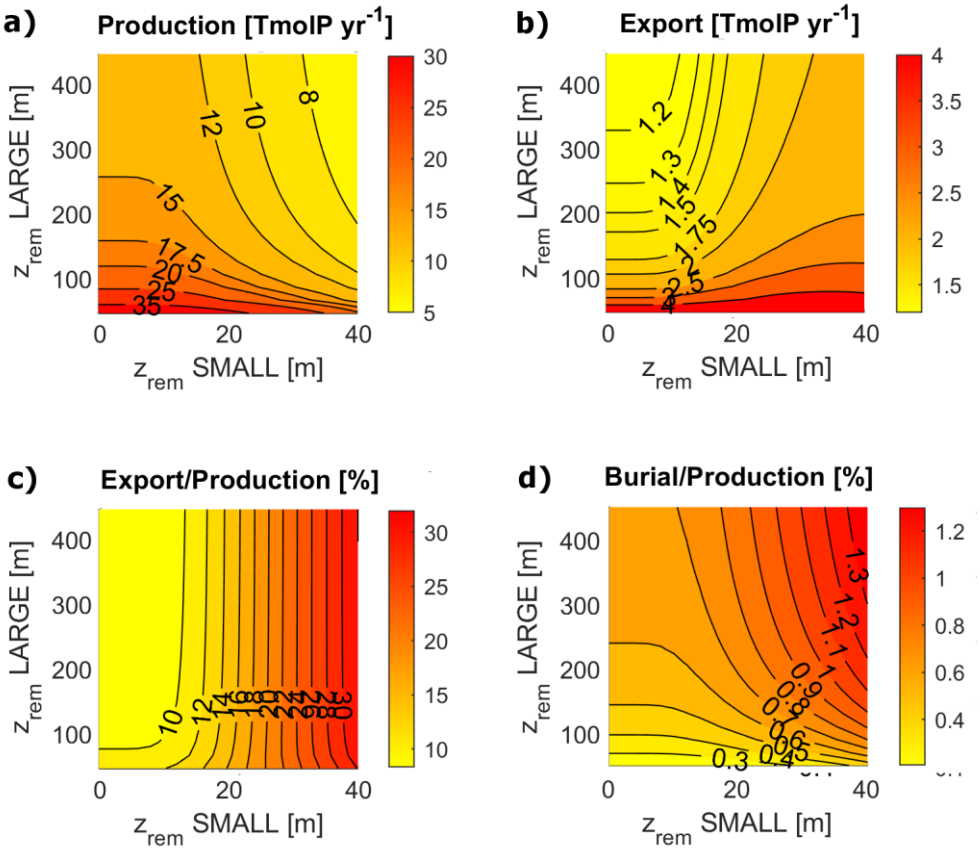

Figure 7: Biological pump fluxes in P units for the entire ocean for varying z_{rem}^{S} and z_{rem}^{L}: (a) P_{org} surface production; (b) P_{org} export through the euphotic layer depth; (c) Export production, i.e. export to production ratio (d) Burial to production ratio.

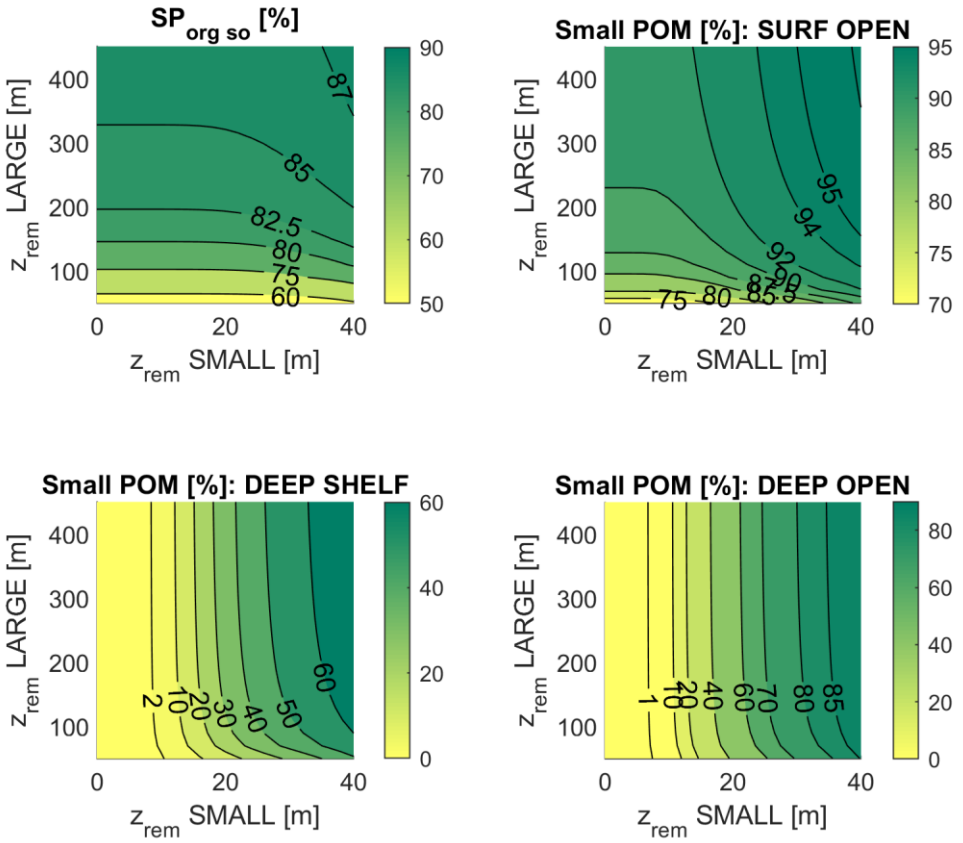

Figure 8: Small P_{org} (SP_{org}) fraction after coagulation in the surface and at depth for varying z_{rem}^{S} and z_{rem}^{L}: (a) surface shelf sea, ss; (b) surface open ocean, so; (c) deep shelf sea, ds; (d) deep open ocean, do.

Appendix A: Equations

A.1 Air-sea gas exchange of oxygen

$$N_{Sch} = 1638 - 81.83 \cdot T_{mean} + 1.483 \cdot {T_{mean}}^2 - 0.008004 \cdot {T_{mean}}^3 \quad \text{(A1)}$$

$$K_W = 0.31 \cdot {W_{speed}}^2 \cdot \sqrt{660/N_{Sch}} \cdot 10^{-2} \cdot (24 \cdot 365.25); \quad \text{(A2)}$$

A.2 Surface shelf sea (ss)

$$V^{ss} = \Delta Z_{eu} \cdot A_{ocean} \cdot \mathcal{P}_{shelf} \quad \text{(A3)}$$

$$Prod^{ss} = P_{eff} \cdot (P^{ss}/(P^{ss} + K_P)) \cdot P^{ss} \quad \text{(A4)}$$

$${SP_{org}}^{ss} = Prod^{ss} - cg_r \cdot (Prod^{ss})^2 \quad \text{(A5)}$$

$${LP_{org}}^{ss} = cg_r \cdot (Prod^{ss})^2 \quad \text{(A6)}$$

$${VExp\_SP_{org}}^{ss} = {SP_{org}}^{ss} \cdot exp(-(\Delta Z_{eu}/2)/z_{rem}^S) \quad \text{(A7)}$$

$${VExp\_LP_{org}}^{ss} = {LP_{org}}^{ss} \cdot exp(-(\Delta Z_{eu}/2)/z_{rem}^L) \quad \text{(A8)}$$

$$\boldsymbol{\frac{dP^{ss}}{dt}} = P_{in} \cdot \left(1 - \mathcal{P}_{open}\right)/V^{ss} + (Upw \cdot (P^{ds} - P^{ss}) + Mix_{ls} \cdot (P^{so} - P^{ss}) + Mix_{vs} \cdot (P^{ds} - P^{ss})) \cdot spy/V^{ss} - \left({\mathrm{VExp}_{\mathrm{SP_{org}}}}^{\mathrm{ss}} + {\mathrm{VExp}_{\mathrm{LP_{org}}}}^{\mathrm{ss}}\right) \quad \text{(A9)}$$

$$AirSea^{ss} = K_W \cdot (O^{at}/K_{Henri} - O^{ss}) \cdot (A_{ocean} \cdot \mathcal{P}_{shelf})/V^{ss} \quad \text{(A10)}$$

$$OProd^{ss} = OP_{Red} \cdot \left({VExp_{SP_{org}}}^{ss} + {VExp_{LP_{org}}}^{ss}\right) \quad \text{(A11)}$$

$$\boldsymbol{\frac{dO^{ss}}{dt}} = \left(Upw \cdot (O^{ds} - O^{ss}) + \mathrm{Mix}_{ls} \cdot (O^{so} - O^{ss}) + \mathrm{Mix}_{vs} \cdot (O^{ds} - O^{ss})\right) \cdot spy/V^{ss} + AirSea^{ss} + OProd^{ss} \quad \text{(A12)}$$

A.3 Deep shelf sea (ds)

$$V^{ds} = \Delta Z_{ds} \cdot A_{ocean} \cdot \mathcal{P}_{shelf} \quad \text{(A13)}$$

$$VInp\_SP_{org}{}^{ds} = VExp\_SP_{org}{}^{ss} \cdot (V^{ss}/V^{ds}) \quad \text{(A14)}$$

$$SP_{org}{}^{ds} = VInp\_SP_{org}{}^{ds} - cg_r \cdot (VInp\_SP_{org}{}^{ds})^2 \quad \text{(A15)}$$

$$LP_{org}{}^{ds} = VExp\_LP_{org}{}^{ss} \cdot (V^{ss}/V^{ds}) + cg_r \cdot (VInp\_SP_{org}{}^{ds})^2 \quad \text{(A16)}$$

$$Rem\_SP_{org}{}^{ds} = SP_{org}{}^{ds} \cdot (1 - exp(-\Delta Z_{ds}/z^S_{rem})) \quad \text{(A17)}$$

$$Rem\_LP_{org}{}^{ds} = LP_{org}{}^{ds} \cdot (1 - exp(-\Delta Z_{ds}/z^L_{rem})) \quad \text{(A18)}$$

$$AerRem\_SedP_{org}{}^{ds} = rm_r \cdot SedP_{org}{}^{s}/\Delta Z_{ds} \cdot (O^{ds}/(O^{ds} + K^s_O)) \quad \text{(A19)}$$

$$AnaRem\_SedP_{org}{}^{ds} = (rm_r \cdot fe_{an}) \cdot SedP_{org}{}^{s}/\Delta Z_{ds} \cdot (1 - O^{ds}/(O^{ds} + K^s_O)) \quad \text{(A20)}$$

$$\frac{\boldsymbol{dP^{ds}}}{\boldsymbol{dt}} = (Upw \cdot (P^{do} - P^{ds}) + Mix_{ld} \cdot (P^{do} - P^{ds}) + Mix_{vs} \cdot (P^{ss} - P^{ds})) \cdot spy/V^{ds} + \left(Rem\_SP_{org}{}^{ds} + Rem\_LP_{org}{}^{ds} + AerRem\_SedP_{org}{}^{ds} + AnaRem\_SedP_{org}{}^{ds}\right) \quad \text{(A21)}$$

$$AerRemWcO^{ds} = OP_{Red} \cdot (Rem\_SP_{org}{}^{ds} + Rem\_LP_{org}{}^{ds}) \cdot (O^{ds}/(O^{ds} + K^w_O)) \quad \text{(A22)}$$

$$AerRemSedO^{ds} = OP_{Red} \cdot AerRem\_SedP_{org}{}^{ds} \quad \text{(A23)}$$

$$\frac{\boldsymbol{dO^{ds}}}{\boldsymbol{dt}} = (Upw \cdot (O^{do} - O^{ds}) + Mix_{ld} \cdot (O^{do} - O^{ds}) + Mix_{vs} \cdot (O^{ss} - O^{ds})) \cdot spy/V^{ds} - AerRemWcO^{ds} - AerRemSedO^{ds} \quad \text{(A24)}$$

A.4 Surface open ocean (so)

$$V^{so} = \Delta Z_{eu} \cdot A_{ocean} \cdot (1 - \mathcal{P}_{shelf}) \quad \text{(A25)}$$

$$Prod^{so} = P_{eff} \cdot (P^{so}/(P^{so} + K_P)) \cdot P^{so} \quad \text{(A26)}$$

$$SP_{org}{}^{so} = Prod^{so} - cg_r \cdot (Prod^{so})^2 \quad \text{(A27)}$$

$$LP_{org}{}^{so} = cg_r \cdot Prod^{so\,2} \quad \text{(A28)}$$

$$VExp\_SP_{org}{}^{so} = SP_{org}{}^{so} \cdot exp(-(\Delta Z_{eu}/2)/z^S_{rem}) \quad \text{(A29)}$$

$$VExp\_LP_{org}{}^{so} = LP_{org}{}^{so} \cdot exp(-(\Delta Z_{eu}/2)/z^L_{rem}) \quad \text{(A30)}$$

$$\frac{\boldsymbol{dP^{so}}}{\boldsymbol{dt}} = P_{in} \cdot \mathcal{P}_{open}/V^{ss} + (Upw \cdot (P^{ss} - P^{so}) + Mix_{ls} \cdot (P^{ss} - P^{so}) + Mix_{vo} \cdot (P^{do} - P^{so})) \cdot spy/V^{so} - \left(VExp\_SP_{org}{}^{so} + VExp\_LP_{org}{}^{so}\right) \quad \text{(A31)}$$

$$AirSea^{so} = K_W \cdot (O^{at}/K_{Henri} - O^{so}) \cdot (A_{ocean} \cdot (1 - \mathcal{P}_{shelf}))/V^{so} \quad \text{(A32)}$$

$$OProd^{so} = OP_{Red} \cdot \left(VExp\_SP_{org}{}^{so} + VExp\_LP_{org}{}^{so}\right) \quad \text{(A33)}$$

$$\frac{\boldsymbol{dO^{so}}}{\boldsymbol{dt}} = \left(Upw \cdot (O^{ss} - O^{so}) + Mix_{ls} \cdot (O^{ss} - O^{so}) + Mix_{vo} \cdot (O^{do} - O^{so})\right) \cdot spy/V^{so} + AirSea^{so} + OProd^{so} \quad \text{(A34)}$$

A.5 Deep open ocean (do)

$$V^{do} = \Delta Z_{do} \cdot A_{ocean} \cdot (1 - \mathcal{P}_{shelf}) \quad \text{(A35)}$$

$$VInp\_SP_{org}{}^{do} = VExp\_SP_{org}{}^{so} \cdot (V^{so}/V^{do}) \quad \text{(A36)}$$

$$SP_{org}{}^{do} = VInp\_SP_{org}{}^{do} - cg_r \cdot (VInp\_SP_{org}{}^{do})^2 \quad \text{(A37)}$$

$$LP_{org}{}^{do} = VExp\_LP_{org}{}^{so} \cdot (V^{so}/V^{do}) + cg_r \cdot (VInp_{SP_{org}}{}^{do})^2 \quad \text{(A38)}$$

$$Rem\_SP_{org}{}^{do} = SP_{org}{}^{do} \cdot (1 - exp(-\Delta Z_{do}/z_{rem}^{S})) \quad \text{(A39)}$$

$$Rem\_LP_{org}{}^{do} = LP_{org}{}^{do} \cdot (1 - exp(-\Delta Z_{do}/z_{rem}^{L})) \quad \text{(A40)}$$

$$AerRem\_SedP_{org}{}^{do} = rm_r \cdot SedP_{org}{}^{o}/\Delta Z_{do} \cdot (O^{do}/(O^{do} + K_O^s)) \quad \text{(A41)}$$

$$AnaRem\_SedP_{org}{}^{do} = (rm_r \cdot fe_{an}) \cdot SedP_{org}{}^{o}/\Delta Z_{do} \cdot (1 - O^{do}/(O^{do} + K_O^s)) \quad \text{(A42)}$$

$$\frac{\boldsymbol{dP^{do}}}{\boldsymbol{dt}} = (Upw \cdot (P^{so} - P^{do}) + Mix_{ld} \cdot (P^{ds} - P^{do}) + Mix_{vo} \cdot (P^{so} - P^{do})) \cdot spy/V^{do} + \left(Rem\_SP_{org}{}^{do} + Rem\_LP_{org}{}^{do} + AerRem\_SedP_{org}{}^{do} + AnaRem\_SedP_{org}{}^{do}\right) \quad \text{(A43)}$$

$$AerRemWcO^{do} = OP_{Red} \cdot (Rem\_SP_{org}{}^{do} + Rem\_LP_{org}{}^{do}) \cdot (O^{do}/(O^{do} + K_O^w)) \quad \text{(A44)}$$

$$AerRemSedO^{do} = OP_{Red} \cdot AerRem\_SedP_{org}{}^{do} \quad \text{(A45)}$$

$$\frac{\boldsymbol{dO^{do}}}{\boldsymbol{dt}} = (Upw \cdot (O^{so} - O^{do}) + Mix_{ld} \cdot (O^{ds} - O^{do}) + Mix_{vo} \cdot (O^{so} - O^{do})) \cdot spy/V^{do} - AerRemWcO^{do} - AerRemSedO^{do} \quad \text{(A46)}$$

A.6 Shelf sea sediments (s)

$$SedFlx^{s} = \left({SP_{org}}^{ds} \cdot exp(-\Delta Z_{ds} / z_{rem}^{S}) + {LP_{org}}^{ds} \cdot exp(-\Delta Z_{ds} / z_{rem}^{L}) \right) \cdot \Delta Z_{ds} \quad \text{(A47)}$$

$$CaPform^{s} = CaP_r \cdot ({SedP_{org}}^{s})^2 \cdot \left(O^{ds}/(O^{ds} + K_O^w) + fs_{an} \cdot (1 - O^{ds}/(O^{ds} + K_O^w)) \right) \quad \text{(A48)}$$

$${Rem\_SedP_{org}}^{ds} = {AerRem\_SedP_{org}}^{ds} + {AnaRem\_SedP_{org}}^{ds} \quad \text{(A49)}$$

$$\frac{d{SedP_{org}}^{s}}{dt} = SedFlx^{s} - CaPform^{s} - {Rem\_SedP_{org}}^{ds} \cdot \Delta Z_{ds} \quad \text{(A50)}$$

A.7 Open ocean sediments (o)

$$SedFlx^{o} = \left({SP_{org}}^{do} \cdot exp(-\Delta Z_{do} / z_{rem}^{S}) + {LP_{org}}^{do} \cdot exp(-\Delta Z_{do} / z_{rem}^{L}) \right) \cdot \Delta Z_{do} \quad \text{(A51)}$$

$$CaPform^{o} = CaP_r \cdot ({SedP_{org}}^{o})^2 \cdot \left(O^{do}/(O^{do} + K_O^w) + fs_{an} \cdot (1 - O^{do}/(O^{do} + K_O^w)) \right) \quad \text{(A52)}$$

$${Rem\_SedP_{org}}^{do} = {AerRem\_SedP_{org}}^{do} + {AnaRem\_SedP_{org}}^{do} \quad \text{(A53)}$$

$$\frac{d{SedP_{org}}^{o}}{dt} = SedFlx^{o} - CaPform^{o} - {Rem\_SedP_{org}}^{do} \cdot \Delta Z_{do} \quad \text{(A54)}$$

A.8 Atmosphere (at)

$$AirSea^{at} = (AirSea^{ss} + AirSea^{so})/(Mol_{atmo} \cdot 10^3) \quad \text{(A55)}$$

$$AnaRemWc^{ds} = OP_{Red} \cdot ({Rem\_SP_{org}}^{ds} + {Rem\_LP_{org}}^{ds}) \cdot (1 - O^{ds}/(O^{ds} + K_O^w)) \quad \text{(A56)}$$

$$AnaRemWc^{do} = OP_{Red} \cdot ({Rem\_SP_{org}}^{do} + {Rem\_LP_{org}}^{do}) \cdot (1 - O^{do}/(O^{do} + K_O^w)) \quad \text{(A57)}$$

$$AnaRemWc^{at} = (AnaRemWc^{ds} \cdot V^{ds} + AnaRemWc^{do} \cdot V^{do})/(Mol_{atmo} \cdot 10^3) \quad \text{(A58)}$$

$$AnaRemSed^{at} = ({AnaRem\_SedP_{org}}^{ds} \cdot V^{ds} + {AnaRem\_SedP_{org}}^{do} \cdot V^{do})/Mol_{atmo} \quad \text{(A59)}$$

$$OxyWeath = W_0 \cdot \sqrt{O^{at}/Omix_0} \, /Mol_{atmo} \quad \text{(A60)}$$

$$\frac{dO^{at}}{dt} = -AirSea^{at} - AnaRemWc^{at} - OxyWeath \quad \text{(A61)}$$

A.9 Diagnostics: Total budgets of P and O

$$P_{sources} = P_{in} \cdot 10^{-15} \quad \text{(A62)}$$

$$P_{sinks} = \left(CaPform^{s} \cdot A_{ocean} \cdot \mathcal{P}_{shelf} + CaPform^{o} \cdot A_{ocean} \cdot \left(1 - \mathcal{P}_{shelf}\right)\right) \cdot 10^{-15} \quad \text{(A63)}$$

$$\frac{\boldsymbol{dP^{TOT}}}{\boldsymbol{dt}} = P_{sources} - P_{sinks} \quad \text{(A64)}$$

$$O_{sources} = (OProd^{ss} \cdot V^{ss} + OProd^{so} \cdot V^{so}) \cdot 10^{-18} \quad \text{(A65)}$$

$$O_{sinks} = \left((SedRemO^{ds} + AerRem^{ds}) \cdot V^{ds} + (SedRemO^{do} + AerRem^{do}) \cdot V^{do} + OxyWeath \cdot Mol_{atmo}\right) \cdot 10^{-18} \quad \text{(A66)}$$

$$\frac{\boldsymbol{dO^{TOT}}}{\boldsymbol{dt}} = O_{sources} - O_{sinks} \quad \text{(A67)}$$

Bibliography

Acevedo-Trejos, E., Brandt, G., Steinacher, M., and Merico, A.: A glimpse into the future composition of marine phytoplankton communities, Frontiers in Marine Science, 1, 10.3389/fmars.2014.00015, 2014.

Alonso-González, I. J., Arístegui, J., Lee, C., Sanchez-Vidal, A., Calafat, A., Fabrés, J., Sangrá, P., Masqué, P., Hernández-Guerra, A., and Benítez-Barrios, V.: Role of slowly settling particles in the ocean carbon cycle, Geophysical research letters, 37, 2010.

Baker, C. A., Henson, S. A., Cavan, E. L., Giering, S. L., Yool, A., Gehlen, M., Belcher, A., Riley, J. S., Smith, H. E., and Sanders, R.: Slow-sinking particulate organic carbon in the Atlantic Ocean: Magnitude, flux, and potential controls, Global Biogeochemical Cycles, 31, 1051-1065, 2017.

Barrón, C., and Duarte, C. M.: Dissolved organic carbon pools and export from the coastal ocean, Global Biogeochemical Cycles, 29, 1725-1738, 10.1002/2014gb005056, 2015.

Barton, A. D., Pershing, A. J., Litchman, E., Record, N. R., Edwards, K. F., Finkel, Z. V., Kiørboe, T., and Ward, B. A.: The biogeography of marine plankton traits, Ecology Letters, 16, 522-534, 10.1111/ele.12063, 2013.

Boyd, P., and Trull, T.: Understanding the export of biogenic particles in oceanic waters: is there consensus?, Progress in Oceanography, 72, 276-312, 2007.

Boyle, R., Dahl, T., Bjerrum, C., and Canfield, D.: Bioturbation and directionality in Earth's carbon isotope record across the Neoproterozoic–Cambrian transition, Geobiology, 16, 252-278, 2018.

Brocks, J. J., Jarrett, A. J., Sirantoine, E., Hallmann, C., Hoshino, Y., and Liyanage, T.: The rise of algae in Cryogenian oceans and the emergence of animals, Nature, 548, 578, 2017.

Buesseler, K. O., and Boyd, P. W.: Shedding light on processes that control particle export and flux attenuation in the twilight zone of the open ocean, Limnology and Oceanography, 54, 1210-1232, 2009.

Carr, M.-E., Friedrichs, M. A., Schmeltz, M., Aita, M. N., Antoine, D., Arrigo, K. R., Asanuma, I., Aumont, O., Barber, R., and Behrenfeld, M.: A comparison of global estimates of marine primary production from ocean color, Deep Sea Research Part II: Topical Studies in Oceanography, 53, 741-770, 2006.

Cavan, E. L., Trimmer, M., Shelley, F., and Sanders, R.: Remineralization of particulate organic carbon in an ocean oxygen minimum zone, Nature communications, 8, 14847, 2017.

Chavez, F. P., and Messié, M.: A comparison of eastern boundary upwelling ecosystems, Progress in Oceanography, 83, 80-96, 2009.

Cole, S. T., Wortham, C., Kunze, E., and Owens, W. B.: Eddy stirring and horizontal diffusivity from Argo float observations: Geographic and depth variability, Geophysical Research Letters, 42, 3989-3997, 2015.

DeVries, T., and Weber, T.: The export and fate of organic matter in the ocean: New constraints from combining satellite and oceanographic tracer observations, Global Biogeochemical Cycles, 31, 535-555, 10.1002/2016gb005551, 2017.

Fennel, K., Follows, M., and Falkowski, P. G.: The co-evolution of the nitrogen, carbon and oxygen cycles in the Proterozoic ocean, American Journal of Science, 305, 526-545, 2005.

Ganachaud, A., and Wunsch, C.: Improved estimates of global ocean circulation, heat transport and mixing from hydrographic data, Nature, 408, 453, 2000.

Garcia, H. E., Weathers, K., Paver, C. R., Smolyar, I., Boyer, T. P., Locarnini, R. A., Zweng, M. M., Mishonov, A. V., Baranova, O. K., Seidov, D., and J. R. Reagan: World Ocean Atlas 2018, Volume 3: Dissolved Oxygen, Apparent Oxygen Utilization, and Oxygen Saturation, A. Mishonov Technical Ed., https://www.nodc.noaa.gov/OC5/woa18/pubwoa18.html, 2018a.

Garcia, H. E., Weathers, K., Paver, C. R., Smolyar, I., Boyer, T. P., Locarnini, R. A., Zweng, M. M., Mishonov, A. V., Baranova, O. K., Seidov, D., and J. R. Reagan: World Ocean Atlas 2018, Volume 4: Dissolved Inorganic Nutrients (phosphate, nitrate and nitrate+nitrite, silicate), A. Mishonov Technical Ed., https://www.nodc.noaa.gov/OC5/woa18/pubwoa18.html, 2018b.

Gruber, N., Friedlingstein, P., Field, C. B., Valentini, R., Heimann, M., Richey, J. E., Lankao, P. R., Schulze, E.-D., and Chen, C.-T. A.: The vulnerability of the carbon cycle in the 21st century: An assessment of carbon-climate-human interactions, Scope-Scientific committee on problems of the environment international council of scientific unions, 62, 45-76, 2004.

Gruber, N., Frenzel, H., Doney, S. C., Marchesiello, P., McWilliams, J. C., Moisan, J. R., Oram, J. J., Plattner, G.-K., and Keith D. Stolzenbach: Eddy-resolving simulation of plankton ecosystem dynamics in the California Current System, Deep Sea Research Part I: Oceanographic Research Papers, 53, 1483-1516, 2006.

Henson, S. A., Sanders, R., Madsen, E., Morris, P. J., Le Moigne, F., and Quartly, G. D.: A reduced estimate of the strength of the ocean's biological carbon pump, Geophysical Research Letters, 38, 2011.

Higgins, M. B., Robinson, R. S., Husson, J. M., Carter, S. J., and Pearson, A.: Dominant eukaryotic export production during ocean anoxic events reflects the importance of recycled NH₄⁺, Proceedings of the National Academy of Sciences, 109, 2269-2274, 10.1073/pnas.1104313109, 2012.

Inthorn, M., Wagner, T., Scheeder, G., and Zabel, M.: Lateral transport controls distribution, quality, and burial of organic matter along continental slopes in high-productivity areas, Geology, 34, 205-208, 10.1130/g22153.1, 2006.
Iversen, M., and Ploug, H.: Ballast minerals and the sinking carbon flux in the ocean: carbon-specific respiration rates and sinking velocity of marine snow aggregates, Biogeosciences 7:, 2613-2624, 2010.
Iversen, M. H., and Poulsen, L. K.: Coprorhexy, coprophagy, and coprochaly in the copepods Calanus helgolandicus, Pseudocalanus elongatus, and Oithona similis, Marine Ecology Progress Series, 350, 79-89, 2007.
Jackson, G. A., and Burd, A. B.: Simulating aggregate dynamics in ocean biogeochemical models, Progress in Oceanography, 133, 55-65, 2015.
Karakaş, G., Nowald, N., Schäfer-Neth, C., Iversen, M., Barkmann, W., Fischer, G., Marchesiello, P., and Schlitzer, R.: Impact of particle aggregation on vertical fluxes of organic matter, Progress in Oceanography, 83, 331-341, 2009.
Katz, M. E., Finkel, Z. V., Grzebyk, D., Knoll, A. H., and Falkowski, P. G.: Evolutionary Trajectories and Biogeochemical Impacts of Marine Eukaryotic Phytoplankton, Annual Review of Ecology, Evolution, and Systematics, 35, 523-556, 10.1146/annurev.ecolsys.35.112202.130137, 2004.
Katz, M. E., Fennel, K., and Falkowski, P. G.: Geochemical and biological consequences of phytoplankton evolution, in: Evolution of primary producers in the sea, Elsevier, 405-430, 2007.
Keeling, R. F., Körtzinger, A., and Gruber, N.: Ocean Deoxygenation in a Warming World, Annual Review of Marine Science, 2, 199-229, 10.1146/annurev.marine.010908.163855, 2010.
Klausmeier, C. A., Litchman, E., and Levin, S. A.: Phytoplankton growth and stoichiometry under multiple nutrient limitation, Limnology and oceanography, 49, 1463-1470, 2004.
Krumhardt, K. M., Callnan, K., Roache-Johnson, K., Swett, T., Robinson, D., Reistetter, E. N., Saunders, J. K., Rocap, G., and Moore, L. R.: Effects of phosphorus starvation versus limitation on the marine cyanobacterium Prochlorococcus MED4 I: uptake physiology, Environmental Microbiology, 15, 2114-2128, 10.1111/1462-2920.12079, 2013.
Kwon, E. Y., Primeau, F., and Sarmiento, J. L.: The impact of remineralization depth on the air–sea carbon balance, Nature Geoscience, 2, 630, 2009.
Lam, P. J., Doney, S. C., and Bishop, J. K. B.: The dynamic ocean biological pump: Insights from a global compilation of particulate organic carbon, CaCO3, and opal concentration profiles from the mesopelagic, Global Biogeochemical Cycles, 25, 10.1029/2010gb003868, 2011.
Laufkötter, C., John, J. G., Stock, C. A., and Dunne, J. P.: Temperature and oxygen dependence of the remineralization of organic matter, Global Biogeochemical Cycles, 31, 1038-1050, 2017.
Lenton, T. M., and Watson, A. J.: Redfield revisited: 1. Regulation of nitrate, phosphate, and oxygen in the ocean, Global Biogeochemical Cycles, 14, 225-248, 2000.
Lenton, T. M., Boyle, R. A., Poulton, S. W., Shields-Zhou, G. A., and Butterfield, N. J.: Co-evolution of eukaryotes and ocean oxygenation in the Neoproterozoic era, Nature Geoscience, 7, 257, 2014.
Lenton, T. M., and Daines, S. J.: Biogeochemical transformations in the history of the ocean, Annual Review of Marine Science, 9, 31-58, 2017.
Lenton, T. M., and Daines, S. J.: The effects of marine eukaryote evolution on phosphorus, carbon and oxygen cycling across the Proterozoic–Phanerozoic transition, Emerging Topics in Life Sciences, 2, 267-278, 2018.
Lenton, T. M., Daines, S. J., and Mills, B. J.: COPSE reloaded: an improved model of biogeochemical cycling over Phanerozoic time, Earth-science reviews, 178, 1-28, 2018.
Lin, S., Litaker, R. W., and Sunda, W. G.: Phosphorus physiological ecology and molecular mechanisms in marine phytoplankton, Journal of Phycology, 52, 10-36, 10.1111/jpy.12365, 2016.
Logan, G. A., Hayes, J., Hieshima, G. B., and Summons, R. E.: Terminal Proterozoic reorganization of biogeochemical cycles, Nature, 376, 53, 1995.
Lomas, M. W., Bonachela, J. A., Levin, S. A., and Martiny, A. C.: Impact of ocean phytoplankton diversity on phosphate uptake, Proceedings of the National Academy of Sciences, 111, 17540-17545, 10.1073/pnas.1420760111, 2014.
Lovecchio, E., Gruber, N., Münnich, M., and Lachkar, Z.: On the long-range offshore transport of organic carbon from the Canary Upwelling System to the open North Atlantic, Biogeosciences, 14, 3337-3369, 2017.
Lu, W., Ridgwell, A., Thomas, E., Hardisty, D. S., Luo, G., Algeo, T. J., Saltzman, M. R., Gill, B. C., Shen, Y., and Ling, H.-F.: Late inception of a resiliently oxygenated upper ocean, Science, 361, 174-177, 2018.
Marsay, C. M., Sanders, R. J., Henson, S. A., Pabortsava, K., Achterberg, E. P., and Lampitt, R. S.: Attenuation of sinking particulate organic carbon flux through the mesopelagic ocean, Proceedings of the National Academy of Sciences, 112, 1089-1094, 2015.
McDonnell, A. M. P., and Buesseler, K. O.: Variability in the average sinking velocity of marine particles, Limnology and Oceanography, 55, 2085-2096, 10.4319/lo.2010.55.5.2085, 2010.
Meyer, A., Sloyan, B. M., Polzin, K. L., Phillips, H. E., and Bindoff, N. L.: Mixing Variability in the Southern Ocean, Journal of Physical Oceanography, 45, 966-987, 10.1175/jpo-d-14-0110.1, 2015.

Meyer, K., Ridgwell, A., and Payne, J.: The influence of the biological pump on ocean chemistry: implications for long-term trends in marine redox chemistry, the global carbon cycle, and marine animal ecosystems, Geobiology, 14, 207-219, 2016.
Moore, J. K., Doney, S. C., and Lindsay, K.: Upper ocean ecosystem dynamics and iron cycling in a global three-dimensional model, Global Biogeochemical Cycles, 18, 2004.
Paulmier, A., Kriest, I., and Oschlies, A.: Stoichiometries of remineralisation and denitrification in global biogeochemical ocean models, Biogeosciences, 6, 923-935, 2009.
Petit, J.-R., Jouzel, J., Raynaud, D., Barkov, N. I., Barnola, J.-M., Basile, I., Bender, M., Chappellaz, J., Davis, M., and Delaygue, G.: Climate and atmospheric history of the past 420,000 years from the Vostok ice core, Antarctica, Nature, 399, 429, 1999.
Ploug, H.: Small-scale oxygen fluxes and remineralization in sinking aggregates, Limnology and Oceanography, 46, 1624-1631, 2001.
Polovina, J. J., Mitchum, G. T., and Evans, G. T.: Decadal and basin-scale variation in mixed layer depth and the impact on biological production in the Central and North Pacific, 1960-88, Deep Sea Research Part I: Oceanographic Research Papers, 42, 1701-1716, 1995.
Ridgwell, A.: Evolution of the ocean's "biological pump", Proceedings of the National Academy of Sciences, 108, 16485-16486, 2011.
Riley, J., Sanders, R., Marsay, C., Le Moigne, F. A., Achterberg, E. P., and Poulton, A.: The relative contribution of fast and slow sinking particles to ocean carbon export, Global Biogeochemical Cycles, 26, 2012.
Rivkin, R. B., and Legendre, L.: Biogenic Carbon Cycling in the Upper Ocean: Effects of Microbial Respiration, Science, 291, 2398-2400, 10.1126/science.291.5512.2398, 2001.
Sarmiento, J. L., and Gruber, N.: Ocean Biogeochemical Dynamics, Princeton University Press, Princeton 2006.
Sharples, J., Middelburg, J. J., Fennel, K., and Jickells, T. D.: What proportion of riverine nutrients reaches the open ocean?, Global Biogeochemical Cycles, 31, 39-58, 10.1002/2016gb005483, 2017.
Slomp, C., and Van Cappellen, P.: The global marine phosphorus cycle: sensitivity to oceanic circulation, Biogeosciences Discussions, 3, 1587-1629, 2006.
Stukel, M. R., and Ducklow, H. W.: Stirring up the biological pump: Vertical mixing and carbon export in the Southern Ocean, Global Biogeochemical Cycles, 31, 1420-1434, 2017.
Sydeman, W. J., García-Reyes, M., Schoeman, D. S., Rykaczewski, R. R., Thompson, S. A., Black, B. A., and Bograd, S. J.: Climate change and wind intensification in coastal upwelling ecosystems, Science, 345, 77-80, 10.1126/science.1251635, 2014.
Tantanasarit, C., Englande, A. J., and Babel, S.: Nitrogen, phosphorus and silicon uptake kinetics by marine diatom Chaetoceros calcitrans under high nutrient concentrations, Journal of experimental marine biology and ecology, 446, 67-75, 2013.
Watson, A. J., Lenton, T. M., and Mills, B. J. W.: Ocean deoxygenation, the global phosphorus cycle and the possibility of human-caused large-scale ocean anoxia, Philosophical Transactions of the Royal Society A: Mathematical, Physical and Engineering Sciences, 375, 20160318, doi:10.1098/rsta.2016.0318, 2017.
Wilson, S. E., Steinberg, D. K., and Buesseler, K. O.: Changes in fecal pellet characteristics with depth as indicators of zooplankton repackaging of particles in the mesopelagic zone of the subtropical and subarctic North Pacific Ocean, Deep Sea Research Part II: Topical Studies in Oceanography, 55, 1636-1647, 2008.
Wollast, R.: Evaluation and comparison of the global carbon cycle in the coastal zone and in the open ocean, The sea, 10, 213-252, 1998.